Levels of ^{187}Au: A detailed study of shape coexistence in an odd-mass nucleus

D. Rupnik and E. F. Zganjar
Department of Physics and Astronomy, Louisiana State University, Baton Rouge, Louisiana 70803

J. L. Wood
School of Physics, Georgia Institute of Technology, Atlanta, Georgia 30332

P. B. Semmes
Department of Physics, Tennessee Technological University, Cookeville, Tennessee 38505

P. F. Mantica*
UNISOR, Oak Ridge Institute of Science and Education, Oak Ridge, Tennessee 37831

(Received 2 December 1997)

The decays of ^{187}Hg (2.2 min; $J^{\pi}=13/2^{+}$) and ^{187}Hg (2.4 min; $J^{\pi}=3/2^{-}$) have been studied with mass-separated sources at the UNISOR facility. Multiscaled spectra of γ rays, x rays, and conversion electrons, as well as $\gamma\gamma t$, $\gamma x t$, $e\gamma t$, and ext coincidences were obtained. Decay schemes have been constructed incorporating $>99\%$ of the decay intensities assigned to the high-spin and low-spin decays. The γ-ray gated conversion-electron spectra permitted determination of 367 conversion coefficients. A variety of coexisting band structures are established in ^{187}Au. Some of these have near-identical analogs in the heavier odd-mass Au isotopes. The remaining bands reveal new degrees of freedom at low excitation energy in ^{187}Au. Nine electric monopole ($E0$) transitions are observed to deexcite members of these new bands. The work represents an undertaking to achieve a benchmark in *complete* spectroscopy following radioactive decay. The most notable band structure in ^{187}Au has two bands with identical spins, nearly identical relative energies, and electric monopole transitions connecting the *favored* members. These bands can be understood as $\pi h_{9/2}$ and $\pi f_{7/2}$ intruder configurations coupled to coexisting prolate or near-prolate ($\gamma \leqslant 20°$) cores having diabatic configurations that differ only in the number of protons occupying the $N=5$ intruder configurations. [S0556-2813(98)02408-X]

PACS number(s): 21.10.Re, 21.60.−n, 23.20.−g, 27.70.+q

I. INTRODUCTION

The nuclei in the far-from-β-stability region defined by $Z \geqslant 78$, $N \leqslant 108$ have become the most extensively characterized region of low-energy shape coexistence known (see, e.g., [1–3]). The Au ($Z=79$) isotopes in this region, in particular, have been the subject of recent radioactive decay studies [4–6], in-beam γ-ray spectroscopy studies [7–11], atomic hyperfine spectroscopy studies [12–14], and low-temperature nuclear orientation studies [15]. In broad terms, the basic features of the shape coexistence in the Au isotopes have been elucidated [5,6,16]. However, detailed studies of the shape coexistence in the Au isotopes have been lacking. The present study describes a detailed experimental and theoretical investigation of the low-lying low-medium spin states in ^{187}Au. (Some selected details of the present study have already been reported [17].)

The nucleus ^{187}Au has been studied previously by radioactive decay [18–22] and by in-beam γ-ray spectroscopy [7,9,10,23]. There are also atomic-beam magnetic resonance data [24] and, as noted, atomic hyperfine spectroscopy information [12,13] that establish the ^{187}Au ground-state spin and magnetic moment. The main features of ^{187}Au have been discussed in terms of the systematic trends seen in the heavier odd-mass Au isotopes [6] and in terms of a pattern of $E0$ transitions which is common to ^{185}Au and ^{187}Au [5]. Besides the much higher statistics of the present study compared to the previous studies [18–22] of ^{187}Hg β decay, we made a dedicated study of the β decay of the low-spin ($T_{1/2}=2.4$ min, $J^{\pi}=3/2^{-}$) ground state ^{187}Hg. This latter experiment entered the $A=187$ mass chain at ^{187}Tl which decays predominantly [25,26] to the low-spin ^{187}Hg β-decaying state.

A major goal of the present study was completeness, i.e., identifying all levels up to a given excitation energy and spin/parity in ^{187}Au. We focused on this issue in a recent study [4] of ^{189}Au. The situation is similar in ^{187}Au, and both ^{189}Hg and ^{187}Hg exhibit high- and low-spin β-decaying isomers which populate states in the spin range $1/2 \leqslant J \leqslant 17/2$. Completeness is crucial for establishing systematics between stability-line nuclei, where detailed spectroscopic information is available, and nuclei far from β stability. A major motivation for the recent study [4] of ^{189}Au was to establish a systematic base for the present investigation of ^{187}Au. The present theoretical studies play a crucial role in this respect: they confront the detailed experimental level scheme with a reliable picture of the density of states, and conversely, the detailed level scheme unequivocally dictates the shape coexisting degrees of freedom in the description of ^{187}Au.

*Current address: Michigan State University, East Lansing, MI 48824.

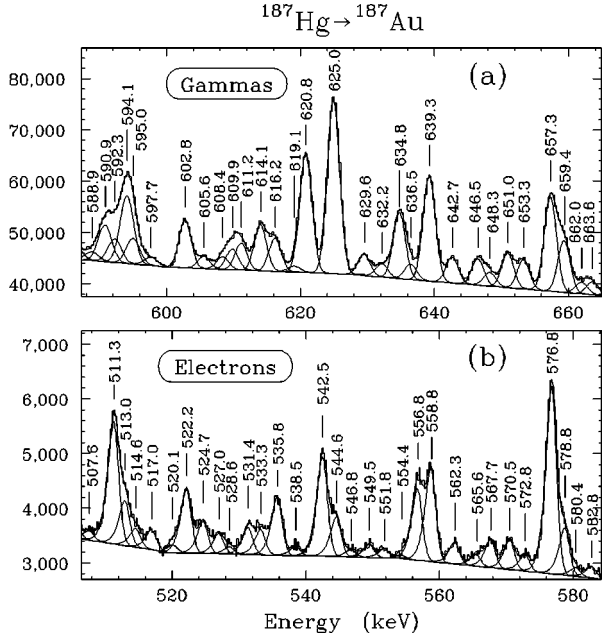

FIG. 1. A portion of the γ-ray (a) and conversion-electron (b) spectra, from the $^{187}Hg^{m}\rightarrow{}^{187}Au$ experiment, analyzed by the code SAM [29]. Peak energies are given in keV. The conversion-electron energies are shifted by the Au K-shell binding energy of 80.7 keV so that the Au γ-ray and K-shell conversion-electron energies are aligned. The fit resulted in 30 γ-ray peaks compared to a detailed coincidence analysis which revealed 45 transitions in this energy region.

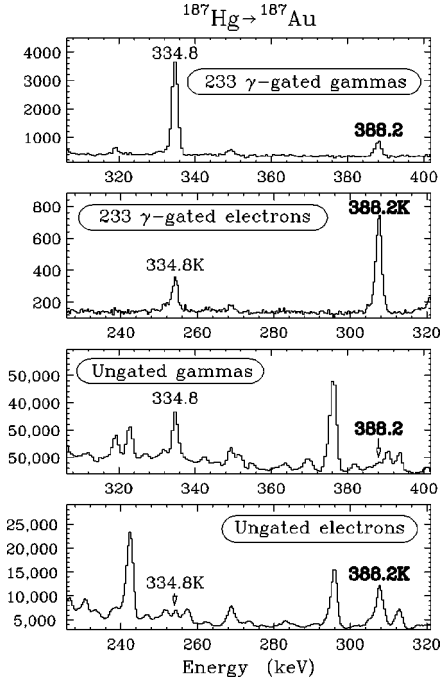

FIG. 2. A portion of background-subtracted gated and ungated conversion-electron and γ-ray spectra, from the $^{187}Hg^{m}\rightarrow{}^{187}Au$ experiment, showing the 388.2 and 334.8 keV transitions. The 388.2 keV transition has $M1(+E2)$ multipolarity with a sizable $E0$ component, which can be compared to the 334.8 keV transition that has $E2$ multipolarity.

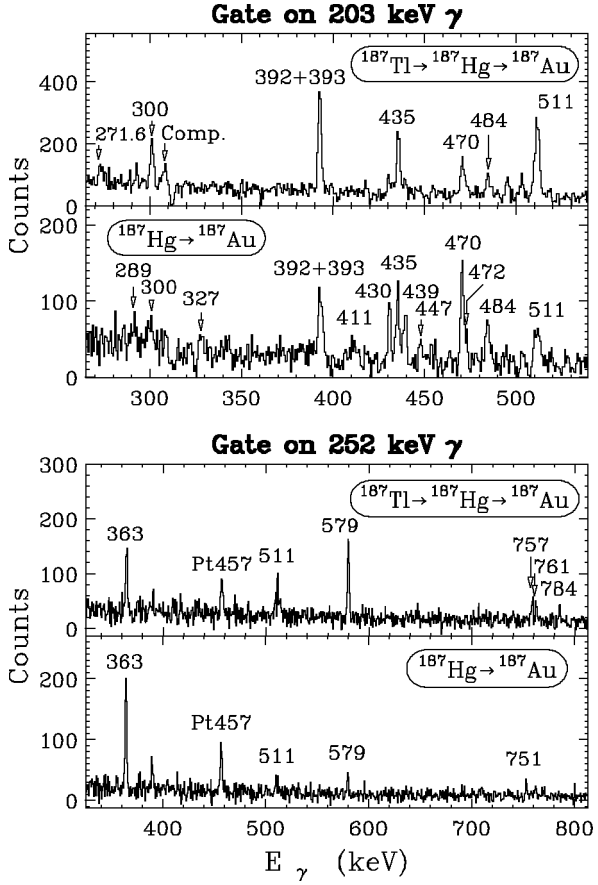

FIG. 3. Background-subtracted gates on the 203 keV (top) and the 252 keV (bottom) transitions, from the $\gamma\gamma$ coincidence data from the $^{187}Hg^{m}\rightarrow{}^{187}Au$ and $^{187}Hg^{m,g}\rightarrow{}^{187}Au$ experiments, respectively. The 392 and 579 keV transitions depopulate levels with spin/parities $3/2^{+}$ and $3/2^{-}$, respectively, and are stronger in the $^{187}Hg^{m,g}\rightarrow{}^{187}Au$ experiment while the 470 and 363 keV transitions depopulate levels with spin/parities $9/2^{+}$ and $9/2^{-}$, respectively, and are stronger in the $^{187}Hg^{m}\rightarrow{}^{187}Au$ experiment.

II. EXPERIMENTAL PROCEDURE

Mass-separated samples of $^{187}Hg^{m}$ were produced by the ^{176}Hf ($^{16}O,5n$) reaction with subsequent mass separation on line with the University Isotope Separator at Oak Ridge (UNISOR). The reaction was initiated by bombarding a HfC target (^{176}Hf enrichment 76%) with 125 MeV $^{16}O^{6+}$ ions at the Holifield Heavy Ion Research Facility (HHIRF) in Oak Ridge, Tennessee. Mass-separated samples of $^{187}Hg^{g}$ were obtained from the radioactive decay of $^{187}Tl^{m,g}$ (15 s, 51 s) following the ^{176}Hf ($^{19}F,8n$) reaction and mass separation using the UNISOR separator. The reaction was produced by bombarding the HfC target with 170 MeV $^{19}F^{8+}$ ions. Targets were bombarded in the UNISOR ion source [27]. Sources were collected on a tape and moved by a compact tape transport system [28] to detector stations. Conventional γ-ray and conversion-electron multiscaling and $\gamma\gamma t$, $e\gamma t$, $\gamma x t$, and ext coincidence spectroscopy were carried out using large volume Ge(Li) detectors and a liquid N_2-cooled 3 mm$\times$200 mm^2 Si(Li) detector. The coincidence data were recorded event by event on magnetic tape, along with the time delay between the two energy pulses. The tapes were scanned subsequently for selected energy and time gates.

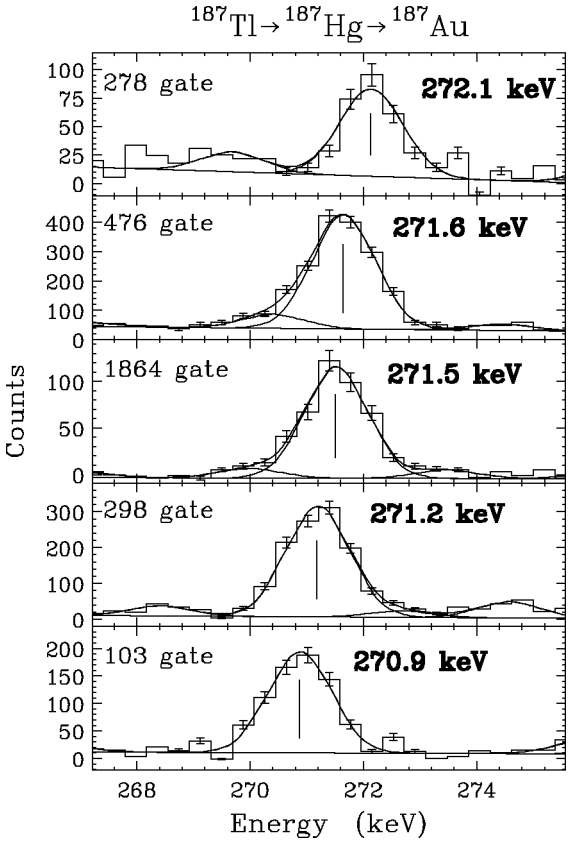

FIG. 4. Five different background-subtracted gates, from the ^{187}Hg$^{g}\rightarrow{}^{187}$Au experiment, showing different members of the 271 keV multiplet.

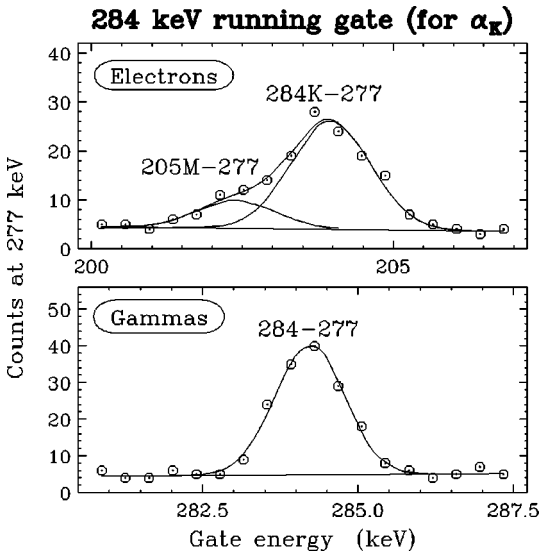

FIG. 5. Running gate across the 284 keV γ rays (upper) and 284K (203 keV) conversion electrons (lower), done on the data from the ^{187}Hg$^{g}\rightarrow{}^{187}$Au experiment. The 277 keV transition was chosen as a ''response'' transition for the plots. Each point in the plot represents the area (counts) of the 277 keV transition, taken from a one-channel gated spectrum. The one-channel windows run across the 284 keV transition in the γ-ray and conversion-electron spectra. The peak at lower energy than the 284K-277 coincidence relation arises from the indirect coincidence between the 205.4 keV M-shell conversion electrons and the 276.6 keV γ rays (through the 130.4 keV transition). The bottom part of the figure shows the same response for γ-gated gammas, where the 205-277 relation cannot be seen because of the chosen energy range.

The systems were calibrated for energy and intensity of γ rays with an absolutely calibrated mixed source (containing ^{125}Sb, ^{154}Eu, and ^{155}Eu), and for energy and intensity of conversion electrons with a mixed ^{133}Ba-^{207}Bi source. Typical source-to-detector distances were 1 cm, and 180° coincidence counting geometries were used. The time-to-amplitude converter (TAC) spectra for both the $\gamma\gamma$ and γe coincidence measurements exhibited a full width at half maximum (FWHM) of $\approx$20 ns. Time gates were set with $\approx$100 ns widths, resulting in true-to-chance ratios $\geqslant$32:1 for the $\gamma\gamma$ coincidences. Gamma-ray spectra covered the range 20–2470 keV. Conversion-electron spectra covered the range 5–1600 keV. Further details can be found in [25].

III. EXPERIMENTAL RESULTS

In Fig. 1(a), a portion of the γ-ray singles spectrum for ^{187}Hg^{m} is shown for the energy range 587–665 keV taken with a detector which had a resolution of 1.9 keV FWHM at 1333 keV. In Fig. 1(b), a portion of the conversion-electron singles spectrum for ^{187}Hg^{m} is shown covering the energy range 506–584 keV taken with a cooled 3 mm$\times$200 mm^2 Si(Li) detector (resolution 1.9 keV FWHM at 975 keV). These spectra were accumulated from 832 sources, each of which was collected for 99 s. The only contaminating lines seen in the spectra are from the daughter decays ^{187}Au (8.4 min), ^{187}Pt (2.35 h), and ^{187}Ir (10.5 h), together with background. These lines were identified using multiscaled data, $\gamma\gamma$, γx, $e\gamma$, and ex coincidences, and comparison with information in Nuclear Data Sheets [30]. The strongest sum peak in the Ge(Li) detector, from the 233.4 keV and 334.8 keV coincident γ rays, is $\approx$4% of the 334.8 keV γ-ray intensity. At the level of precision reported for relative intensities in this work, summing has a negligible effect. No summing was seen in the Si(Li) detector.

Spectra for ^{187}Hg^{g} were accumulated from 1325 sources, each of which was collected for 120 s. Because the ^{187}Hg^{g} production was achieved via ^{187}Tl^{m,g} (51 s, 16 s) β^+/EC decay, contamination from this decay occurred. Also, direct production of ^{187}Hg^{m} occurred via the ^{176}Hf(^{19}F, $p7n$) reaction. Lines from ^{187}Tl^{m,g} decay were identified by comparing spectra taken at two sequential counting stations; i.e., each source was counted for 120 s at ''station 1'' and then moved to ''station 2'' where it was counted for 120 s (while the next source was being counted at station 1). Comparison of ^{187}Tl lines, so identified, was made with data from a separate experiment [26]. The ^{187}Hg^{m} lines were straightforwardly deconvoluted from the ^{187}Hg^{g} spectrum. Summing was similar to that observed in the ^{187}Hg^{m} spectra.

Representative spectra from the $\gamma\gamma t$ and $e\gamma t$ coincidences are shown in Figs. 2 and 3. Figure 3 also shows the difference between spectra from ^{187}Hg^{m} and ^{187}Hg^{g} decay using the same gating transition. This will be discussed later. The $\gamma\gamma t$ coincidences were taken at counting station 2 and the $e\gamma t$ coincidences were taken at counting station 1. It was possible to identify x-ray lines uniquely in nearly all coincidence gates, providing a confirmation of our assignment of γ rays and conversion electrons to ^{187}Hg$^{m,g}\rightarrow{}^{187}$Au decays.

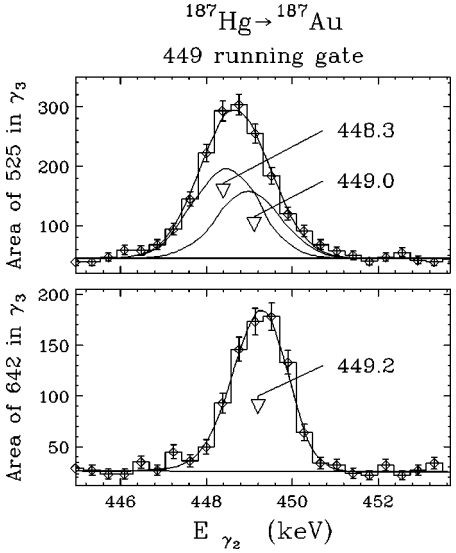

FIG. 6. Plot of the running gate across the energy of 449 keV with the area of the total 525 keV peak as a response transition (upper part) and the area of the 642 keV peak as a response transition (lower part). The upper plot reveals two pairs of coincident transitions while the lower plot has only one. (The 449.0 keV line in coincidence with the 525 keV transition is due to the same transition as the 449.2 keV line in coincidence with the 642 keV transition: the energy difference results because the line fits are independent and it reflects the errors in the method.)

Spurious events due to Compton backscattering and summing were identified and eliminated. Coincidence intensities were extracted for all lines seen in the selected coincidence gates. The extraction of coincidence intensities was essential because of the complexity of the decays. For example, Fig. 4 shows evidence for a 271.5 keV quintuplet. In fact, the energies and intensities of γ-ray and conversion-electron lines obtained from the analyses of the singles spectra were of limited use because of this complexity. For example, in the energy range depicted in Fig. 1, spectrum fitting resulted in 30 γ-ray lines, whereas analysis of the coincidence data identified 45 γ-ray lines in this energy range. Further, many lines from $^{187}Hg^{m,g}\rightarrow{}^{187}Au$ are doublets with lines from $^{187}Au\rightarrow{}^{187}Pt$. The singles data were primarily used to establish overall relative intensities of the strongest lines.

Another method in the coincidence analysis used to separate multiplets is that of ''running gates'' [25]. For example, in a two-dimensional array, one runs a one-channel gate along one axis (spectrum A) and thus scans a peak of interest to generate a coincidence spectrum (spectrum B). The area (counts) of the ''response'' line in spectrum B, which is in coincidence with the specified coincident peak in spectrum A, is then determined for each of the gated spectra and plotted as a function of the energy of the gate channel from spectrum A. For example, in Fig. 5, gates were ''run'' across the region containing a line at 284 keV in spectrum A and the area (counts) of the 277 keV transition in spectrum B for each gate were plotted as a function of the gate energy. Thus, the image of the peak in spectrum A, which is in coincidence with a given peak in spectrum B, was generated. This was done for both γet and $\gamma\gamma t$ data. This method can extract accurate internal-conversion coefficients α_K from complex spectra (cf. Fig. 5). The 284 keV gamma line is not a singlet. Careful coincidence analysis reveals that the 284 keV gamma line is a triplet in ^{187}Au, and is also contaminated by 284 keV transitions from ^{187}Hg, ^{187}Pt, and ^{187}Ir. The running gate technique removes all transitions from the multiplet peak at the gate energy except the one that is in coincidence with the response line (277 keV in this case). As a result, it was possible in this case to obtain sufficient precision in α_K so that the 284 keV transition in coincidence with the 277 keV line could be identified as $E0+M1(+E2)$. Another example of a running gate is shown in Fig. 6. This shows the existence of the coincidence doublet 448.3/525.4 and 449.2/524.5 keV, which is discussed later.

The vast majority of conversion-coefficient measurements were obtained from a comparison of γ-gated gamma and γ-gated electron spectra [25]. An example is presented in Fig. 2, which shows a portion of gated (top two spectra) and ungated (bottom two spectra) γ-ray and conversion-electron spectra. Note that by gating both the γ-ray and conversion-electron spectra with the 233 keV transition, one can extract relative conversion coefficients for the 334.8 and 388.2 keV transitions. In this case, it is determined that $\alpha_K=0.05(1)$ for the 334.8 keV transition and $\alpha_K=0.96(11)$ for the 388.2 keV transition. Normalization of the conversion-electron spectra was done using the 233.4 keV transition seen in beam and assigned as a $13/2^-\rightarrow 9/2^-$ yrast transition [8–10]. (The present work uniquely confirms its placement.) Thus, the normalization uses the theoretical [31] $E2$ α_K for the 233.4 keV transition. The theoretical value for α_K for an $E2$ transition at 334.8 keV is 0.05 (indicating pure $E2$ multipolarity for this transition) and the theoretical value for α_K for an $M1$ transition at 388.2 keV is 0.14 (cf. above); therefore, the 388.2 keV transition has an α_K value which is 6 times larger than the theoretical value for $M1$. Since prompt coincidences are inconsistent with transitions of high multipolarity ($M2$, $E3$, etc.), a sizable $E0$ component must be present in the 388.2 keV transition. In this way, transitions containing $E0$ enhancement are identified. The two lower plots in Fig. 2 are presented to show the advantage of gated spectra compared to the ungated coincidence spectra. In order to obtain accurate intensities and therefore accurate internal-conversion coefficients, more than 2000 gates were extracted in this analysis.

The heavy-ion reactions used in the two experiments produced both ground ($I^\pi=3/2^-$) and metastable ($I^\pi=13/2^+$) states of the ^{187}Hg nucleus, which each decay through β^+/EC to the states of ^{187}Au. Since there is no isomeric transition ($13/2^+\rightarrow 3/2^-$), the relative intensity of a specific transition in ^{187}Au is the sum of the intensities resulting from the concurrent $^{187}Hg^g$ and $^{187}Hg^m$ EC/β^+ decays. Relative amounts of $^{187}Hg^g$ and $^{187}Hg^m$ produced in each reaction can be roughly expressed using the intensity of two transitions: 233.4 keV as a high-spin signature and 203.4 keV as a (predominantly) low-spin signature. If the relative γ-ray intensity for the 233.4 keV transition is normalized to a 100 units in both reactions, the 203.4 keV transition has a relative γ-ray intensity of 47 units in the experiment using 170 MeV ^{19}F and 12 units in the experiment using 125 MeV ^{16}O on ^{176}Hf, respectively. The procedure to separate transition intensities is relatively straightforward and is presented in detail in Ref. [25].

TABLE I. Gamma and electron intensities in ^{187}Au for ^{187}Hg^{g} decay. An asterisk indicates $I_\gamma(203.4)=100$; note 1 is $s_{1/2}\oplus d_{3/2}\oplus d_{5/2}$ bands, note 2 $h_{11/2}$ bands, note 3 $h_{9/2}\oplus f_{7/2}$ bands, and note g only in ^{187}Hg^{g} decay; T is total intensity; L12 is the conversion coefficient for L12-shell electrons; and R indicates the running gate method.

E_γ	^{187}Hg^{g} decay		α_K	Theory [31]		Multipolarity	I_i	I_f	E_i	E_f	Note
(keV)	I_γ (ΔI)*	I_e (ΔI)		$E2$	$M1$				(keV)	(keV)	
19.5							$3/2^+$	$1/2^+$	19.5	0.0	-
36.9	15.(5)T						$5/2^+$	$3/2^+$	240.3	203.4	1-
50.7	21.7(60)T						$5/2^+$	$5/2^+$	291.0	240.3	1-
89.7	0.4(2)	2.8(16)L	7(4)L			E2	$1/2^-$	$5/2^-$	545.9	456.2	3-g
101.0	699.(55)T					E3	$9/2^-$	$3/2^+$	120.5	19.5	-
102.3	0.2(1)	obscured					$3/2^-$	$5/2^-$	428.2	325.9	3-g
103.3	22.5(30)		1.5(5)L12	1.6724	0.9499	76%E2+M1	$1/2^-$	$5/2^-$	275.0	171.8	3-g
103.4	8.7(4)		0.99(8)L12	1.6652	0.9473	81%M1+E2	$11/2^-$	$9/2^-$	223.9	120.5	2-
129.7	0.75(20)	1.5(4)	2.0(7)	0.4550	2.9789		$7/2^+$	$(3/2^+)$	633.7	503.8	1-
130.4	4.0(10)	6.4(12)	1.6(4)	0.4501	2.9335	E2+M1	$5/2^-$	$7/2^-$	456.2	325.9	3-g
138.5	0.49(10)	0.29(12)	0.6(3)	0.3980	2.4711		$7/2^+$	$7/2^+$	633.7	495.6	1-
142.7	0.6(2)	0.30(15)	0.5(3)	0.3735	2.2700	E2+M1	$7/2^-$	$5/2^-$	597.8	456.2	3-g
153.3	17.8(22)	9.8(15)	0.55(17)	0.3192	1.8528	E2+M1	$3/2^-$	$1/2^-$	428.2	275.0	3-g
153.7	15.9(19)	20.0(10)	1.32(9)	0.3173	1.8392	M1+E2	$7/2^-$	$5/2^-$	325.9	171.8	3-
156.7	0.5(3)	obscured		0.3025	1.7508	E2	$3/2^-$	$7/2^-$	754.5	597.8	3-g
170.4	0.6(2)	obscured		0.2502	1.3747		$7/2^-$	$3/2^-$	597.8	428.2	3-g
181.4	7.5(20)	1.65(66)	0.22(8)	0.2156	1.1531	E2	$5/2^-$	$1/2^-$	456.2	275.0	3-g
183.7	1.36(60)	0.46(12)	0.34(10)	0.2092	1.1131	85%E2+M1	$3/2^+$	$3/2^+$	203.4	19.5	1-
185.7	3.9(9)	0.27(8)	0.07(2)	E1:	0.0709	E1	$7/2^-$	$5/2^+$	476.4	291.0	2-
192.3	0.9(2)	0.30(12)	0.33(17)	0.1873	0.9793	E2+M1	$5/2^+$	$7/2^+$	687.0	495.6	1-
203.4	100.(7)	80.(9)	0.8(1)	0.1632	0.8373	M1	$3/2^+$	$1/2^+$	203.4	0.0	1-
205.4	42.2(40)	23.6(30)	0.56(10)	0.1593	0.8148	E2+M1	$7/2^-$	$9/2^-$	325.9	120.5	3-
208.4	3.5(7)	1.6(9)	0.46(21)R	0.1527	0.7771	(M1+E2)	$3/2^-$	$1/2^-$	754.5	545.9	3-g
220.8	47.6(32)	9.7(14)	0.203(29)	0.1333	0.6665	88%E2+M1	$5/2^+$	$3/2^+$	240.3	19.5	1-
236.3	5.7(4)	0.28(7)	0.05(2)	E1:	0.0393	E1	$7/2^-$	$5/2^+$	476.4	240.3	2-
240.3	66.(5)	7.9(12)	0.12(2)	0.1080	0.5274	E2	$5/2^+$	$1/2^+$	240.3	0.0	1-
252.5	21.1(30)	1.9(3)	0.09(2)	0.0955	0.4602	E2	$7/2^-$	$11/2^-$	476.4	223.9	2-
255.2	6.3(4)	2.5(5)	0.40(6)	0.0930	0.4470	78%M1+E2	$7/2^+$	$5/2^+$	495.6	240.3	1-
256.4	15.7(13)	2.8(8)	0.18(6)	0.0922	0.4427	E2+M1	$3/2^-$	$5/2^-$	428.2	171.8	3-g
263.8	2.0(5)	1.1(4)	0.53(20)R	0.0857	0.4081	(M1)	$(3/2^+)$	$5/2^+$	503.8	240.3	1-g
270.9	19.9(25)	11.7(23)	0.59(7)R	0.0802	0.3795	E0+M1(+E2)	$1/2^-$	$1/2^-$	545.9	275.0	3-g
271.5	83.(8)	34.9(65)	0.42(8)	0.0800	0.3783	M1+E2	$5/2^+$	$3/2^+$	291.0	19.5	1-
272.1	3.3(6)	1.2(2)	0.37(8)R	0.0793	0.3745	M1	$7/2^-$	$7/2^-$	597.8	325.9	3-
275.4	2.7(5)	0.30(6)	0.11(3)	0.0770	0.3628	76%E2+M1		$(3/2^+)$	778.6	503.8	1-g
276.6	4.8(7)	1.9(5)	0.4(1)	0.0762	0.3585	(M1)	$5/2^-$	$5/2^-$	732.5	456.2	3-g
278.7	4.2(6)	1.5(3)	0.36(7)	0.0748	0.3512	M1	$5/2^-$	$7/2^-$	876.8	597.8	3-g
284.5	18.4(21)	9.6(19)	0.52(6)R	0.0711	0.3320	E0+M1(+E2)	$5/2^-$	$5/2^-$	456.2	171.8	3-g
291.0	1.9(6)	obscured		0.0673	0.3121		$5/2^+$	$1/2^+$	291.0	0.0	1-
292.2	0.9(2)	0.06(2)	0.07(2)	0.0666	0.3087	E2	$7/2^+$	$3/2^+$	495.6	203.4	1-
298.4	5.8(8)	1.2(6)	0.21(15)	0.0628	0.2894	M1+E2	$3/2^-$	$5/2^-$	754.5	456.2	3-g
299.6	3.0(5)	0.39(10)	0.13(7)	0.0626	0.2884	M1+E2	$3/2^+$	$5/2^+$	590.9	291.0	1-
300.3	4.2(2)	0.34(17)	0.08(4)	0.0623	0.2866	(E2+M1)	$(3/2^+)$	$3/2^+$	503.8	203.4	1-g
304.5	1.8(2)	0.45(18)	0.25(15)	0.0602	0.2760	(M1)	$3/2^+$	$5/2^+$	595.3	291.0	1-g
326.2	6.30(75)	1.32(30)	0.21(5)	0.0507	0.2279	M1	$3/2^-$	$3/2^-$	754.5	428.2	3-g
327.0	0.9(1)	0.14(7)	0.16(9)	0.0506	0.2275	M1+E2	$5/2^+$	$7/2^+$	822.7	495.6	1-
330.9	4.2(4)	obscured		0.0492	0.2204		$5/2^-$	$1/2^-$	876.8	545.9	3-g
335.7	3.3(9)	obscured		0.0475	0.2120		$5/2^-$	$9/2^-$	456.2	120.5	3-g
342.6	1.5(3)	0.20(6)	0.13(4)	0.0453	0.2007	E2+M1	$7/2^+$	$5/2^+$	633.7	291.0	1-
347.9	1.1(2)	0.22(6)	0.20(7)	0.0437	0.1925	(M1)	$5/2^+$	$5/2^+$	638.9	291.0	1-g
350.0	1.5(3)	0.15(7)	0.10(6)	0.0430	0.1895	(M1+E2)	$3/2^+$	$5/2^+$	590.9	240.3	1-
355.3	2.1(6)	0.42(14)	0.20(8)	0.0415	0.1820	(M1)	$3/2^+$	$5/2^+$	595.3	240.3	1-g
374.2	26.(4)	1.0(6)	0.04(2)	0.0367	0.1584	(E2)	$1/2^-$	$5/2^-$	545.9	171.8	3-g
387.7	0.9(2)	0.20(6)	0.22(8)R	0.0338	0.1441	(E0+M1(+E2))	$3/2^+$	$3/2^+$	590.9	203.4	1-
391.9	8.4(15)	1.7(3)	0.20(3)R	0.0330	0.1400	(E0+M1(+E2))	$3/2^+$	$3/2^+$	595.3	203.4	1-g
393.4	14.2(6)	2.1(3)	0.15(3)	0.0327	0.1386	M1	$7/2^+$	$5/2^+$	633.7	240.3	1-

The data presented here for ^{187}Au represent only a subset of the observed levels and transitions. A specification of the energy ''cutoff,'' above which levels and their depopulating transitions are not shown, is stated in the captions for the decay schemes (Figs. 7–13). The omitted levels and transitions are given in Ref. [25].

Tables I and II list the transition energies E_γ, the separated relative γ-ray intensities I_γ, the conversion-electron intensities I_e, experimental K-shell (and some L-shell) internal-conversion coefficients α_K, theoretical internal-conversion coefficients for $E2$, $E1$, and $M1$ multipolarity from Rösel *et al.* [31], assigned multipolarities, initial and

TABLE I. (*Continued*).

E_γ	$^{187}Hg^g$ decay		α_K	Theory [31]		Multipolarity	I_i	I_f	E_i	E_f	Note
(keV)	I_γ (ΔI)*	I_e (ΔI)		$E2$	$M1$				(keV)	(keV)	
395.9	1.2(3)	0.17(5)	0.14(6)R	0.0322	0.1362	M1	$5/2^+$	$5/2^+$	687.0	291.0	1-
398.3	6.6(5)	1.4(5)	0.21(10)	0.0318	0.1341	>M1	$5/2^+$	$5/2^+$	638.9	240.3	1-g
402.1	3.3(6)	0.26(13)	0.08(5)	0.0311	0.1307	(M1+E2)		$1/2^-$	948.0	545.9	3-g
407.8	7.8(5)	0.94(19)	0.12(3)	0.0301	0.1259	M1	$5/2^-$	$7/2^-$	732.5	325.9	3-g
421.5	4.2(5)	0.42(6)	0.10(2)	0.0279	0.1153	(M1)	$5/2^-$	$5/2^-$	876.8	456.2	3-g
426.1	14.(2)	1.3(3)	0.09(2)	0.0272	0.1121	M1+E2	$7/2^-$	$5/2^-$	597.8	171.8	3-
428.6	2.7(9)	0.07(4)	0.026(15)	0.0268	0.1103	E2	$3/2^-$	$7/2^-$	754.5	325.9	3-g
429.5	1.8(5)	0.22(7)	0.12(4)	0.0267	0.1097	(M1)	$3/2^-$	$1/2^-$	975.3	545.9	3-g
429.9	1.8(3)	0.045(22)	0.025(15)	0.0267	0.1095	(E2)	$7/2^+$	$3/2^+$	633.7	203.4	1-
435.5	9.(1)	0.7(1)	0.078(12)	0.0259	0.1058	M1+E2	$5/2^+$	$3/2^+$	638.9	203.4	1-g
446.9	3.0(2)	0.27(7)	0.09(3)	0.0244	0.0988	M1	$5/2^+$	$5/2^+$	687.0	240.3	1-
457.8	9(2)	0.36(29)	0.04(3)	0.0231	0.0927	(E2)	$5/2^-$	$1/2^-$	732.5	275.0	3-g
476.0	22.6(21)	0.54(9)	0.024(5)	0.0212	0.0837	E2	$7/2^+$	$3/2^+$	495.6	19.5	1-
478.0	11.4(5)	0.57(19)	0.05(2)	0.0210	0.0827	E2+M1	$7/2^-$	$9/2^-$	597.8	120.5	3-
480.1	3.6(5)	0.22(6)	0.06(2)	0.0208	0.0818	M1+E2	$3/2^-$	$1/2^-$	754.5	275.0	3-g
483.7	2.4(3)	0.07(2)	0.03(1)	0.0205	0.0802	E2(+M1)	$5/2^+$	$3/2^+$	687.0	203.4	1-
484.3	6.9(9)	0.55(18)	0.08(3)	0.0204	0.0799	M1	$(3/2^+)$	$3/2^+$	503.8	19.5	1-g
503.6	9.3(4)	0.7(3)	0.08(4)	0.0187	0.0722	(M1)	$(3/2^+)$	$1/2^+$	503.8	0.0	1-g
519.4	2.1(5)	0.15(7)	0.07(4)	0.0175	0.0666	M1	$3/2^-$	$5/2^-$	975.3	456.2	3-g
545.9	5.1(9)	0.041(25)	0.008(3)	E1:	0.0060	E1	$1/2^-$	$1/2^+$	545.9	0.0	3-g
551.8	2.1(9)	0.11(5)	0.05(3)	0.0154	0.0568	M1	$5/2^-$	$7/2^-$	876.8	325.9	3-g
571.4	9.6(15)	0.28(5)	0.029(5)	0.0143	0.0519	M1+E2	$3/2^+$	$3/2^+$	590.9	19.5	1-
575.8	2.9(7)	0.26(15)	0.09(6)	0.0141	0.0509	>M1 (E0?)	$3/2^+$	$3/2^+$	595.3	19.5	1-g
579.3	7.8(6)	0.15(8)	0.019(10)	0.0139	0.0501	(E2)	$3/2^-$	$7/2^-$	1056.0	476.4	2-g
582.4	3.0(2)	0.13(2)	0.043(7)	0.0137	0.0494	M1+E2	$5/2^+$	$5/2^+$	822.7	240.3	1-
582.6	1.9(6)	obscured		0.0137	0.0494		$3/2^-$	$5/2^-$	754.5	171.8	3-g
591.0	3.3(5)	0.17(6)	0.05(2)	0.0133	0.0476	M1	$3/2^+$	$1/2^+$	590.9	0.0	1-
595.2	2.4(7)	0.12(5)	0.05(2)	0.0131	0.0467	(M1)	$3/2^+$	$1/2^+$	595.3	0.0	1-g
614.1	3.0(14)	0.09(2)	0.03(2)	0.0123	0.0431		$7/2^+$	$3/2^+$	633.7	19.5	1-
618.7	0.75(30)	0.04(1)	0.05(2)	0.0121	0.0422	M1	$5/2^+$	$3/2^+$	822.7	203.4	1-
619.0	3.0(5)	0.15(5)	0.05(2)	0.0121	0.0422	(M1)	$5/2^+$	$3/2^+$	638.9	19.5	1-g
638.7	3.4(5)	<0.3(2)	<0.09(6)	0.0113	0.0389		$5/2^+$	$1/2^+$	638.9	0.0	1-g
667.8	2.4(3)	0.10(3)	0.04(2)	0.0104	0.0347	M1	$5/2^+$	$3/2^+$	687.0	19.5	1-
686.7	0.9(2)	obscured		0.0098	0.0323		$5/2^+$	$1/2^+$	687.0	0.0	1-
700.3	15.1(15)	0.45(6)	0.030(4)	0.0094	0.0307	M1	$3/2^-$	$1/2^-$	975.3	275.0	3-g
745.2	2.1(2)	0.025(8)	0.012(5)	0.0083	0.0262	E2+M1		$1/2^-$	1291.1	545.9	3-g
757.3	2.9(4)	0.032(15)	0.011(6)	0.0080	0.0252	(E2+M1)		$7/2^-$	1233.7	476.4	2-g
761.0	3.5(5)	0.07(2)	0.020(7)	0.0080	0.0248	(M1)	$5/2^-$	$7/2^-$	1237.5	476.4	2-g
764.4	1.5(3)	too weak		E1:	0.0031		$3/2^-$	$5/2^+$	1056.0	291.0	2-g
783.8	2.2(4)	0.018(12)	0.008(4)	0.0075	0.0230	(E2)	$3/2^-$	$7/2^-$	1260.2	476.4	2-g
791.0	3.3(2)	0.17(8)	0.05(3)	0.0074	0.0225	>M1 (E0?)		$3/2^+$	994.4	203.4	1-g
803.5	1.1(2)	0.010(4)	0.009(4)	0.0072	0.0216	E2+M1	$3/2^-$	$5/2^-$	975.3	171.8	3-g
816.1	2.4(4)	too weak		E1:	0.0027		$3/2^-$	$5/2^+$	1056.0	240.3	2-g
853.3	3.0(4)	too weak		E1:	0.0025		$3/2^-$	$3/2^+$	1056.0	203.4	2-g
1036.1	2.7(9)	0.008(6)	0.003(2)	E1:	0.0017	(E1)	$3/2^-$	$1/2^+$	1056.0	19.5	2-g
1056.0	7.5(23)	0.015(5)	0.0020(8)	E1:	0.0017	(E1)	$3/2^-$	$1/2^+$	1056.0	0.0	2-g

final state spins, and initial and final state energies for the transitions from the $^{187}Hg^g$ and $^{187}Hg^m$ decay, respectively. In the $^{187}Hg^g$ decay, all intensities are given relative to the γ-ray intensity of the 203.4 keV transition (100 units), and in the $^{187}Hg^m$ decay all the intensities are given relative to the γ-ray intensity of the 233.4 keV transition (100 units). The error in the last reported digits of the intensity is given by the numbers in parentheses.

A comparison of the present results for the $^{187}Hg^{g,m}$ decay and the work of Bourgeois *et al.* [18] and Grimm [19] is restricted by the fact that neither of these other studies separated the two decays, as is done here. Also, while we have identified 526 transitions and 228 levels in ^{187}Au, Bourgeois *et al.* identified only 71 and 34, respectively, and Grimm 179 and 96, respectively. The nuclear Data Sheets for $A=187$ [30] base their ^{187}Hg decay scheme on the work of Bourgeois *et al.* [18].

IV. DECAY SCHEMES

A partial decay scheme for 2.4 min $^{187}Hg^g \rightarrow {}^{187}$Au is presented in Figs. 7–9. Its construction relies almost completely on the coincidence data. In total, we have established excited states up to an energy of 2525 keV in ^{187}Au from the $^{187}Hg^g$ β decay. Levels above 1300 keV (42 of them) and their corresponding depopulating transitions (79 of them) are not shown in Figs. 7–9; they can be found in Ref. [25]. Approximately 99% of the total observed decay intensity has been assigned. Except for several levels that are fed directly by β decay and which depopulate directly to the ground state or to

TABLE II. Gamma and electron intensities in ^{187}Au for ^{187}Hg^m decay. An asterisk indicates $I_\gamma(233.4)=100$, note 1 is $s_{1/2}\oplus d_{3/2}\oplus d_{5/2}$ bands, note 2 $h_{11/2}$bands, note 3 $h_{9/2}\oplus f_{7/2}$ bands, and note m only in ^{187}Hg^{m}decay; T is total intensity; L12 is the conversion coefficient for L12-shell electrons; and R indicates running gate method.

E_γ	^{187}Hg^m decay		α_K	Theory [31]		Multipolarity	I_i	I_f	E_i	E_f	Note
(keV)	I_γ (ΔI)*	I_e (ΔI)		$E2$	$M1$				(keV)	(keV)	
19.5							$3/2^+$	$1/2^+$	19.5	0.0	-
36.9	4.7(20)T						$5/2^+$	$3/2^+$	240.3	203.4	1-
50.7	0.9(4)T						$5/2^+$	$5/2^+$	291.0	240.3	1-
51.2	30.(15)T						$5/2^-$	$9/2^-$	171.8	120.5	3-
101.0	678.(50)T					E3	$9/2^-$	$3/2^+$	120.5	19.5	-
103.4	22.0(15)		0.99(8)L12	1.6652	0.9473	81%M1+E2	$11/2^-$	$9/2^-$	223.9	120.5	2-
117.5	0.50(15)	0.34(10)	0.68(21)	0.5476	3.9497	E2+M1	$9/2^-$	$7/2^-$	443.3	325.9	3-m
122.0	0.45(15)	0.45(16)	1.0(4)	0.5116	3.5473	M1+E2	$13/2^-$	$11/2^-$	742.1	619.8	3-m
127.4	0.8(2)	0.56(9)	0.7(2)	0.4712	3.1348	E2+M1	$15/2^-$	$17/2^-$	816.0	688.7	3-m
129.7	0.27(10)	0.54(15)	2.0(7)	0.4550	2.9789		$7/2^+$	$(3/2^+)$	633.7	503.8	1-
131.8	0.55(10)	0.44(9)	0.8(2)	0.4406	2.8456	E2+M1	$11/2^-$	$13/2^-$	881.2	749.3	2-m
133.7	0.7(3)	0.56(12)	0.8(5)	0.4281	2.7319	E2+M1	$9/2^+$	$7/2^+$	767.0	633.7	1-m
135.4	0.45(15)	0.23(11)	0.5(3)	0.4171	2.6354		$7/2^+$	$7/2^+$	1015.0	880.4	1-m
138.5	0.20(10)	0.12(5)	0.6(3)	0.3980	2.4711		$7/2^+$	$7/2^+$	633.7	495.6	1-
140.7	0.15(5)	0.33(8)	2.2(9)	0.3849	2.3629	(M1+E2)	$13/2^-$	$15/2^-$	956.7	816.0	3-m
142.6	2.05(20)	3.9(8)	1.9(5)	0.3741	2.2746	M1(+E2)	$11/2^-$	$13/2^-$	496.8	353.9	3-m
148.3	0.55(20)	too weak		0.3451	2.0469		$17/2^+$	$19/2^-$	1380.8	1232.7	3-m
148.8	1.1(2)	0.33(10)	0.3(1)	0.3410	2.0159	(E2)	$11/2^+$	$7/2^+$	1164.6	1015.0	1-m
153.7	1.1(3)	1.45(8)	1.32(9)	0.3173	1.8392	M1+E2	$7/2^-$	$5/2^-$	325.9	171.8	3-
154.0	0.3(1)	0.12(5)	0.40(18)	0.3160	1.8221	(E2)	$11/2^+$	$7/2^+$	1121.3	965.6	1-m
171.7	0.55(15)	0.19(6)	0.5 (3)	0.2458	1.3456		$11/2^-$	$7/2^-$	496.8	325.9	3-m
176.5	0.3(1)	0.25(8)	1.0 (6)	0.2305	1.2532	M1+E2	$11/2^-$	$9/2^-$	619.8	443.3	3-m
181.0	0.45(10)	0.11(6)	0.24(14)	0.2168	1.1603	E2+M1	$13/2^+$	$11/2^+$	1149.5	968.3	1-m
183.7	0.02(1)	too weak		0.2092	1.1131	85%E2+M1	$3/2^+$	$3/2^+$	203.4	19.5	1-
185.7	0.6(1)	too weak		E1:	0.0709	E1	$7/2^-$	$5/2^+$	476.4	291.0	2-
192.3	0.51(20)	0.17(8)	0.33(17)	0.1873	0.9793	E2+M1	$5/2^+$	$7/2^+$	687.0	495.6	1-
192.6	0.8(2)	0.26(15)	0.33(20)	0.1865	0.9750	(E2+M1)	$7/2^+$	$5/2^+$	880.4	687.0	1-m
196.0	0.65(20)	0.11(8)	0.17(9)	0.1787	0.9285	E2	$15/2^-$	$11/2^-$	816.0	619.8	3-m
196.9	0.8(2)	0.30(7)	0.37(11)	0.1768	0.9167	E2+M1	$11/2^+$	$11/2^+$	1164.6	968.3	1-m
203.4	1.9(6)	1.52(16)	0.8(1)	0.1632	0.8373	M1	$3/2^+$	$1/2^+$	203.4	0.0	1-
205.4	2.8(7)	1.57(20)	0.56(10)	0.1593	0.8148	E2+M1	$7/2^-$	$9/2^-$	325.9	120.5	3-
207.8	0.45(10)	0.07(2)	0.16(6)	0.1548	0.7889	(E2)	$11/2^-$	$15/2^-$	881.2	673.4	2-m
215.3	0.6(1)	0.3(1)	0.50(19)	0.1419	0.7148	M1+E2	$9/2^+$	$7/2^+$	710.7	495.6	1-m
220.8	16.5(20)	3.3(5)	0.203(29)	0.1333	0.6665	88%E2+M1	$5/2^+$	$3/2^+$	240.3	19.5	1-
233.4	100.(4)	11.6(13)	0.116(14)	0.1161	0.5716	E2	$13/2^-$	$9/2^-$	353.9	120.5	3-m
236.3	0.7(1)	too weak		E1:	0.0393	E1	$7/2^-$	$5/2^+$	476.4	240.3	2-
240.3	21.(2)	2.5(4)	0.12(2)	0.1080	0.5274	E2	$5/2^+$	$1/2^+$	240.3	0.0	1-
245.1	1.1(2)	0.29(6)	0.26(6)	0.1028	0.4995	E2+M1	$13/2^-$	$11/2^-$	742.1	496.8	3-m
247.6	1.45(20)	0.36(7)	0.25(8)	0.1003	0.4857	M1+E2	$5/2^+$	$5/2^+$	934.5	687.0	1-m
252.5	3.7(9)	0.33(4)	0.09(2)	0.0955	0.4602	E2	$7/2^-$	$11/2^-$	476.4	223.9	2-
255.2	6.2(3)	2.5(5)	0.40(6)	0.0930	0.4470	78%M1+E2	$7/2^+$	$5/2^+$	495.6	240.3	1-
257.4	1.85(10)	0.31(8)	0.17(4)	0.0910	0.4365	E2+M1	$11/2^+$	$9/2^+$	968.3	710.7	1-m
258.7	0.3(1)	0.15(5)	0.5(2)	0.0899	0.4303	(M1)	$9/2^-$	$11/2^-$	755.4	496.8	3-m
259.2	1.35(20)	0.12(8)	0.09(6)	0.0895	0.4283	E2	$17/2^+$	$13/2^+$	1380.8	1121.8	3-m
265.9	1.1(2)	0.22(8)	0.20(8)	0.0840	0.3993	E2+M1	$11/2^-$	$13/2^-$	619.8	353.9	3-m
271.2	7.5(7)	0.7(2)	0.09(3)	0.0798	0.3772	E2	$9/2^-$	$5/2^-$	443.3	171.8	3-m
271.5	3.3(9)	1.4(3)	0.42(8)	0.0800	0.3783	M1+E2	$5/2^+$	$3/2^+$	291.0	19.5	1-
271.6	4.2(5)	0.55(9)	0.13(3)	0.0797	0.3768	E2+M1	$9/2^+$	$7/2^+$	767.0	495.6	1-m
272.1	0.37(10)	0.14(2)	0.37(8)R	0.0793	0.3745	M1	$7/2^-$	$7/2^-$	597.8	325.9	3-
283.7	2.8(4)	0.76(13)	0.27(4)	0.0716	0.3346	M1+E2	$13/2^+$	$13/2^+$	1405.5	1121.8	3-m
284.2	0.9(2)	0.067(22)	0.075(23)	0.0713	0.3329	E2	$11/2^+$	$7/2^+$	1164.6	880.4	1-m
289.5	1.55(20)	0.16(5)	0.10(4)	0.0681	0.3166	(E2)	$7/2^+$	$3/2^+$	880.4	590.9	1-m
291.0	0.06(2)	obscured		0.0673	0.3121		$5/2^+$	$1/2^+$	291.0	0.0	1-
292.1	0.7(1)	0.02(1)	0.028(14)	E1:	0.0237	E1	$13/2^+$	$11/2^-$	1121.8	829.3	3-m
292.2	0.3(1)	too weak		0.0666	0.3087	E2	$7/2^+$	$3/2^+$	495.6	203.4	1-

the 120.5 or 223.9 keV levels [isomeric with $T_{1/2}=2.3$ s [20] and 48(2) ns [21], respectively] all assignments of transitions and levels in the scheme are supported by coincidence data, with the individual transition intensities being determined from the $\gamma\gamma$ and $e\gamma$ coincidence data. Transitions not in coincidence with any other transition are assumed to go to the ground state or to the 120.5 keV ($J^\pi=9/2^-$) or 223.9 keV ($J^\pi=11/2^-$) isomeric states. (Transitions to the ground state, $J^\pi=1/2^+$, generally depopulate low-spin levels while transitions to either of the isomeric states, $J^\pi=9/2^-$

TABLE II. (*Continued*).

E_γ	$^{187}Hg^m$ decay		α_K	Theory [31]		Multipolarity	I_i	I_f	E_i	E_f	Note
(keV)	I_γ (ΔI)*	I_e (ΔI)		*E*2	*M*1				(keV)	(keV)	
294.5	0.6(1)	0.03(1)	0.05(2)	0.0653	0.3022	E2	$11/2^-$	$7/2^-$	619.8	325.9	3-m
298.6	9.9(4)	0.8(2)	0.08(2)	0.0631	0.2910	E2	$13/2^-$	$9/2^-$	742.1	443.3	3-m
299.6	1.2(2)	0.14(4)	0.13(7)	0.0626	0.2884	M1+E2	$3/2^+$	$5/2^+$	590.9	291.0	1-
304.6	0.4(1)	0.2(1)	0.5(3)	0.0602	0.2758	(M1)	$15/2^-$	$17/2^-$	993.3	688.7	3-m
305.4	1.5(2)	0.05(2)	0.03(1)	E1:	0.0214	(E1)	$13/2^+$	$15/2^-$	1121.8	816.0	3-m
305.8	1.8(2)	0.27(5)	0.15(3)R	0.0596	0.2728	M1+E2	$13/2^-$	$11/2^-$	1187.0	881.2	2-m
319.2	7.0(2)	0.4(1)	0.057(15)	0.0537	0.2429	E2	$15/2^-$	$11/2^-$	816.0	496.8	3-m
322.9	13.4(5)	8.3(10)	0.62(7)	0.0522	0.2354	E0+M1(+E2)	$9/2^-$	$9/2^-$	443.3	120.5	3-m
327.0	0.4(1)	0.06(3)	0.16(9)	0.0506	0.2275	M1+E2	$5/2^+$	$7/2^+$	822.7	495.6	1-
331.8	0.55(20)	0.12(8)	0.22(19)	0.0489	0.2187	(M1)	$13/2^-$	$15/2^-$	1147.8	816.0	3-m
331.9	0.85(10)	0.14(6)	0.17(9)	0.0485	0.2166	M1+E2	$7/2^+$	$7/2^+$	965.6	633.7	1-m
332.3	1.6(2)	0.30(10)	0.19(6)	0.0487	0.2179	M1	$11/2^-$	$11/2^-$	829.3	496.8	3-m
334.8	17.5(3)	0.95(5)	0.054(9)	0.0478	0.2135	E2	$17/2^-$	$13/2^-$	688.7	353.9	3-m
336.7	2.3(1)	0.37(5)	0.16(2)	0.0472	0.2103	E2+M1	$13/2^-$	$11/2^-$	956.7	619.8	3-m
342.6	0.65(10)	0.08(2)	0.13(4)	0.0453	0.2007	E2+M1	$7/2^+$	$5/2^+$	633.7	291.0	1-
342.8	0.7(1)	0.04(2)	0.06(3)	0.0453	0.2005	(E2)	$17/2^-$	$15/2^-$	1158.9	816.0	3-m
343.6	1.25(15)	0.15(4)	0.12(4)	0.0450	0.1991	M1+E2	$5/2^+$	$3/2^+$	934.5	590.9	1-m
349.5	4.5(6)	0.86(9)	0.18(3)R	0.0432	0.1903	M1		$13/2^+$	1471.2	1121.8	3-m
350.0	0.45(9)	0.05(3)	0.10(6)	0.0430	0.1895	(M1+E2)	$3/2^+$	$5/2^+$	590.9	240.3	1-
351.9	0.8(1)	0.16(2)	0.20(3)	0.0425	0.1867	M1		$7/2^-$	950.5	597.8	3-m
360.4	1.3(2)	0.045(9)	0.035(10)	0.0401	0.1751	E2	$9/2^-$	$13/2^-$	1317.1	956.7	3-m
363.3	2.1(2)	0.10(5)	0.05(3)	0.0394	0.1714	(E2+M1)	$9/2^-$	$7/2^-$	840.3	476.4	2-m
364.	0.7(2)	0.07(2)	0.10(4)	0.0392	0.1705	E2+M1	$15/2^-$	$15/2^-$	1357.8	993.3	3-m
366.5	0.95(15)	0.09(3)	0.09(4)	0.0386	0.1675	E2+M1	$9/2^-$		1317.1	950.5	3-m
371.3	1.45(30)	0.07(2)	0.05(2)	0.0374	0.1617	(E2+M1)		$9/2^-$	1126.5	755.4	3-m
373.6	0.95(15)	0.04(1)	0.04(1)	0.0369	0.1590	(E2)	$15/2^-$	$11/2^-$	993.3	619.8	3-m
376.3	41.0(9)	4.9(6)	0.119(15)	0.0363	0.1560	M1+E2	$11/2^-$	$9/2^-$	496.8	120.5	3-m
381.7	0.75(15)	0.10(3)	0.14(5)	0.0351	0.1502	(M1)	$7/2^+$	$7/2^+$	1015.0	633.7	1-m
381.8	0.85(20)	0.05(2)	0.06(3)	0.0351	0.1501	E2(+M1)	$13/2^+$	$9/2^+$	1149.5	767.0	1-m
382.8	1.0(1)	0.03(1)	0.03(1)	0.0348	0.1490	E2	$9/2^+$	$5/2^+$	1205.5	822.7	1-m
384.6	0.85(2)	0.043(9)	0.05(1)	0.0345	0.1472	E2+M1	$7/2^+$	$7/2^+$	880.4	495.6	1-m
385.8	2.3(3)	0.39(10)	0.17(4)	0.0342	0.1460	M1	$11/2^-$	$9/2^-$	829.3	443.3	3-m
387.5	0.50(15)	0.010(5)	0.020(12)	E1:	0.0124	(E1)	$17/2^+$	$15/2^-$	1380.8	993.3	3-m
387.7	0.32(8)	0.07(2)	0.22(8)R	0.0338	0.1441	(E0+M1(+E2))	$3/2^+$	$3/2^+$	590.9	203.4	1-
388.2	3.0(2)	2.9(4)	0.96(11)	0.0337	0.1436	E0+M1(+E2)	$13/2^-$	$13/2^-$	742.1	353.9	3-m
388.5	0.7(1)	0.13(3)	0.18(5)R	0.0337	0.1433	M1	$9/2^-$	$9/2^-$	1228.8	840.3	2-m
392.5	0.55(15)	0.038(20)	0.07(3)	0.0329	0.1394	E2+M1		$11/2^-$	1590.2	1197.6	2-m
393.4	5.1(2)	0.16(3)	0.15(3)	0.0327	0.1386	M1	$7/2^+$	$5/2^+$	633.7	240.3	1-
395.9	0.5(2)	0.07(2)	0.14(6)R	0.0322	0.1362	M1	$5/2^+$	$5/2^+$	687.0	291.0	1-
404.6	0.55(15)	0.017(9)	0.031(18)	0.0306	0.1290	(E2)	$11/2^-$	$7/2^-$	881.2	476.4	2-m
410.6	3.6(2)	0.49(10)	0.135(30)	0.0296	0.1237	M1	$11/2^+$	$9/2^+$	1121.3	710.7	1-m
416.9	0.5(1)	0.02(1)	0.04(2)	0.0286	0.1187	(E2)	$19/2^-$	$15/2^-$	1232.7	816.0	3-m
417.1	0.8(2)	0.032(10)	0.04(2)	0.0286	0.1186	(E2)	$17/2^-$	$13/2^-$	1158.9	742.1	3-m
419.5	0.4(1)	0.016(5)	0.04(2)	0.0282	0.1168	(E2)	$9/2^+$	$5/2^+$	710.7	291.0	1-m
424.1	1.0(2)	0.032(7)	0.032(9)	0.0275	0.1135	(E2)	$7/2^+$	$3/2^+$	1015.0	590.9	1-m
425.0	1.6(4)	0.046(10)	0.029(6)	0.0274	0.1128	(E2)	$17/2^-$	$13/2^-$	1167.1	742.1	3-m
426.1	1.3(1)	0.12(3)	0.09(2)	0.0272	0.1121	M1+E2	$7/2^-$	$5/2^-$	597.8	171.8	3-
429.6	2.1(4)	0.13(4)	0.061(15)	0.0267	0.1097	M1+E2	$9/2^-$	$7/2^-$	755.4	325.9	3-m
429.9	0.6(1)	0.015(7)	0.025(15)	0.0267	0.1095	(E2)	$7/2^+$	$3/2^+$	633.7	203.4	1-
430.2	4.4(1)	0.12(3)	0.027(7)	0.0266	0.1093	E2	$15/2^+$	$11/2^+$	1399.0	968.3	1-m
436.6	1.45(20)	0.10(2)	0.07(2)	0.0257	0.1051	M1+E2	$13/2^-$	$13/2^-$	1393.3	956.7	3-m
437.9	0.4(1)	0.09(2)	0.22(7)	0.0256	0.1043	(E0+M1(+E2))	$13/2^-$	$13/2^-$	1187.0	749.3	2-m
438.8	10.0(3)	0.23(6)	0.023(5)	0.0255	0.1037	E2	$13/2^+$	$9/2^+$	1149.5	710.7	1-m
438.9	1.5(1)	0.06(2)	0.043(15)	0.0254	0.1036	E2+M1	$5/2^+$	$7/2^+$	934.5	495.6	1-m
446.5	2.1(2)	0.11(3)	0.05(1)	0.0245	0.0990	E2+M1		$13/2^+$	1568.3	1121.8	3-m

and $11/2^-$, mostly depopulate higher-spin levels.)

Figure 7 shows the decay scheme (below 1300 keV) for the level structure of the $s_{1/2}\oplus d_{3/2}\oplus d_{5/2}$ bands in ^{187}Au observed through the $^{187}Hg^g$ decay. Using $\alpha_K > \alpha_K^{M1,\mathrm{th}}$ as an indicator for an *E*0 component, the two transitions with clear *E*0 components (387.7 and 391.9 keV) and three for which *E*0 is suggested (398.3, 575.8, and 791.0 keV) connect structures in the $s_{1/2}\oplus d_{3/2}\oplus d_{5/2}$ bands. The scheme of Bourgeois *et al.* [18] up to a spin/parity of $7/2^+$, although it is much less complete, agrees with our work with the exception of two levels. The exceptions are the levels at 496 and 968 keV. Bourgeois *et al.* [18] assign a probable spin/parity of $5/2^+$ to the 496 keV level, while we assign it to be $7/2^+$. They missed the fact that the 476 keV transition to the $3/2^+$

TABLE II. (*Continued*).

E_γ	$^{187}Hg^m$ decay		α_K	Theory [31]		Multipolarity	I_i	I_f	E_i	E_f	Note
(keV)	I_γ (ΔI)*	I_e (ΔI)		*E*2	*M*1				(keV)	(keV)	
446.9	1.5(1)	0.14(3)	0.09(3)	0.0244	0.0988	M1	$5/2^+$	$5/2^+$	687.0	240.3	1-
448.3	4.0(5)	0.24(6)	0.06(3)	0.0242	0.0978	M1+E2	$11/2^-$	$13/2^-$	1197.6	749.3	2-m
449.2	26.0(15)	0.63(15)	0.024(6)	0.0241	0.0973	E2	$15/2^-$	$11/2^-$	673.4	223.9	2-m
450.1	3.5(15)	0.3(2)	0.09(6)	0.0240	0.0972	(M1)		$11/2^-$	674.0	223.9	2-m
455.3	1.55(20)	0.06(4)	0.038(25)	0.0234	0.0941	(E2)	$17/2^+$	$13/2^+$	1604.8	1149.5	1-m
459.4	4.7(2)	0.28(9)	0.06(2)	0.0230	0.0919	E2+M1	$13/2^-$	$11/2^-$	956.7	496.8	3-m
462.1	11.8(6)	0.59(10)	0.050(9)	0.0227	0.0905	60%E2+M1	$15/2^-$	$13/2^-$	816.0	353.9	3-m
467.7	1.0(2)	0.05(1)	0.05(2)	0.0221	0.0876	E2+M1		$13/2^+$	1590.5	1121.8	3-m
470.2	0.9(2)	0.06(2)	0.07(3)	0.0218	0.0864	M1+E2	$17/2^-$	$17/2^-$	1158.9	688.7	3-m
470.3	27.1(5)	0.62(10)	0.023(4)	0.0218	0.0864	E2	$9/2^+$	$5/2^+$	710.7	240.3	1-m
472.8	11.3(2)	0.23(5)	0.020(5)	0.0215	0.0852	E2	$11/2^+$	$7/2^+$	968.3	495.6	1-m
475.4	2.0(3)	0.16(5)	0.08(3)	0.0213	0.0839	M1	$11/2^-$	$13/2^-$	829.3	353.9	3-m
476.0	23.(2)	0.55(9)	0.024(5)	0.0212	0.0837	E2	$7/2^+$	$3/2^+$	495.6	19.5	1-
476.3	3.6(4)	0.08(3)	0.022(9)	0.0212	0.0835	E2	$9/2^+$	$5/2^+$	767.0	291.0	1-m
478.0	0.8(1)	0.04(1)	0.05(2)	0.0210	0.0827	E2+M1	$7/2^-$	$9/2^-$	597.8	120.5	3-
478.1	0.25(10)	0.06(2)	0.24(10)	0.0210	0.0827	E0+M1(+E2)	$17/2^-$	$17/2^-$	1167.1	688.7	3-m
479.6	0.55(10)	0.017(8)	0.03(2)	0.0209	0.0820	(E2)	$9/2^-$	$13/2^-$	1228.8	749.3	2-m
483.7	0.8(2)	0.024(7)	0.03(1)	0.0205	0.0802	E2(+M1)	$5/2^+$	$3/2^+$	687.0	203.4	1-
486.4	1.75(20)	0.04(1)	0.023(6)	0.0202	0.0790	E2	$11/2^+$	$7/2^+$	1121.3	633.7	1-m
487.7	1.4(2)	0.06(2)	0.042(16)	0.0201	0.0785	E2+M1	$9/2^-$	$11/2^-$	984.9	496.8	3-m
494.6	0.7(1)	0.05(1)	0.07(2)	0.0195	0.0757	M1	$9/2^+$	$9/2^+$	1205.5	710.7	1-m
496.5	0.2(1)	obscured		0.0194	0.0751		$15/2^-$	$11/2^-$	993.3	496.8	3-m
499.4	19.6(9)	0.67(10)	0.034(6)	0.0191	0.0738	E2+M1	$11/2^-$	$9/2^-$	619.8	120.5	3-m
501.9	3.1(2)	0.022(9)	0.007(3)	E1:	0.0071	E1	$13/2^+$	$11/2^-$	1121.8	619.8	3-m
503.	0.60(15)	obscured		0.0188	0.0724		$11/2^-$	$7/2^-$	829.3	325.9	3-m
513.	0.55(15)	0.016(6)	0.03(2)	0.0180	0.0688		$13/2^-$	$9/2^-$	956.7	443.3	3-m
513.6	0.75(10)	0.03(1)	0.043(18)	0.0180	0.0685	(E2+M1)	$13/2^-$	$15/2^-$	1187.0	673.4	2-m
520.1	0.75(15)	0.04(1)	0.057(14)	0.0175	0.0663	M1	$7/2^+$	$7/2^+$	1015.0	495.6	1-m
524.5	3.5(4)	0.055(15)	0.016(6)	0.0172	0.0650	E2	$11/2^-$	$15/2^-$	1197.6	673.4	2-m
525.4	24.(1)	1.06(30)	0.044(11)	0.0171	0.0646	M1+E2	$13/2^-$	$11/2^-$	749.3	223.9	2-m
526.7	1.9(2)	0.040(15)	0.021(10)	0.0170	0.0642	(E2)	$9/2^+$	$5/2^+$	767.0	240.3	1-m
527.8	2.2(2)	0.095(20)	0.043(8)	0.0169	0.0638	M1+E2	$13/2^-$	$11/2^-$	1147.8	619.8	3-m
537.3	1.1(1)	0.044(20)	0.04(2)	0.0163	0.0609	M1+E2		$9/2^+$	1304.7	767.0	1-m
537.5	0.8(2)	0.03(1)	0.04(2)	0.0163	0.0609	M1+E2	$13/2^-$	$11/2^-$	1418.2	881.2	2-m
542.0	0.8(2)	0.032(10)	0.04(2)	0.0160	0.0596	M1+E2	$15/2^-$	$15/2^-$	1357.8	816.0	3-m
544.0	0.6(1)	0.03(2)	0.05(3)	0.0159	0.0590	M1(+E2)	$19/2^-$	$17/2^-$	1232.7	688.7	3-m
546.7	0.6(1)	0.036(12)	0.06(3)	0.0158	0.0582	(M1)	$7/2^+$	$5/2^+$	1369.7	822.7	1-m
551.1	0.5(1)	0.02(1)	0.05(3)	0.0151	0.0551 M1		$15/2^-$	$15/2^-$	1368.1	816.0	3-m
564.8	3.75(20)	0.026(9)	0.007(2)	E1:	0.0056	E1	$17/2^+$	$15/2^-$	1380.8	816.0	3-m
566.9	0.5(1)	obscured		0.0145	0.0528		$17/2^-$	$13/2^-$	1316.1	749.3	2-m
569.5	1.2(1)	0.04(1)	0.033(9)	0.0144	0.0524	E2+M1	$11/2^+$	$9/2^+$	1280.8	710.7	1-m
571.4	2.8(2)	0.081(15)	0.029(5)	0.0143	0.0519	M1+E2	$3/2^+$	$3/2^+$	590.9	19.5	1-
578.8	0.7(2)	0.035(11)	0.050(16)	0.0139	0.0502	M1	$13/2^-$	$15/2^-$	1393.3	816.0	3-m
582.4	1.3(1)	0.056(8)	0.043(7)	0.0137	0.0494	M1+E2	$5/2^+$	$5/2^+$	822.7	240.3	1-
583.4	0.4(1)			0.0136	0.0491		$9/2^-$	$5/2^-$	755.4	171.8	3-m
584.4	0.80(15)	0.026(9)	0.033(12)	0.0136	0.0490	M1+E2		$15/2^-$	1400.4	816.0	3-m
586.7	0.95(30)	0.029(9)	0.03(1)	0.0135	0.0485	M1+E2		$7/2^-$	1184.5	597.8	3-m
591.0	0.8(1)	0.040(15)	0.05(2)	0.0133	0.0476	M1	$3/2^+$	$1/2^+$	590.9	0.0	1-
594.2	1.2(1)	0.019(4)	0.016(3)	0.0132	0.0469	E2(+M1)		$9/2^+$	1304.7	710.7	1-m
602.9	2.35(15)	0.068(10)	0.029(5)	0.0128	0.0452	M1+E2	$13/2^-$	$13/2^-$	956.7	353.9	3-m
614.1	1.7(8)	0.05(2)	0.03(2)	0.0123	0.0431		$7/2^+$	$3/2^+$	633.7	19.5	1-
616.4	3.1(3)	0.146(30)	0.047(10)	0.0122	0.0427	M1	$9/2^-$	$11/2^-$	840.3	223.9	2-m
618.7	0.28(5)	0.014(3)	0.05(2)	0.0121	0.0422	M1	$5/2^+$	$3/2^+$	822.7	203.4	1-
621.8	1.7(2)	0.02(1)	0.012(6)	0.0120	0.0417	E2	$13/2^-$	$9/2^-$	742.1	120.5	3-m
624.9	0.25(8)	0.011(9)	0.04(3)	0.0119	0.0412	M1	$15/2^-$	$13/2^-$	1368.1	742.1	3-m

level at 19.5 keV is part of a triplet (not doublet) and that an interfering 478 keV transition has an $E0$ component. The other level improperly assigned, at 968 keV, has spin/parity $11/2^+$ according to our data (and, consequently, is shown as such in Fig. 10), whereas Bourgeois *et al.* [18] assign $7/2^+$. A possible reason for their error could be that they missed the fact that the 472.8 keV depopulating transition is contaminated by a relatively strong ^{187}Pt transition at 471.4 keV the *K*-conversion electrons of which are part of the multiplet at 473 $-B_k^{Z=79}$ keV for 473 Au *K*-conversion electrons. Levels and depopulating transitions above 995 keV can be found in Ref. [25].

Figure 8 shows the decay scheme (below 1300 keV) for the level structure of the $h_{11/2}$ bands in ^{187}Au observed

TABLE II. (*Continued*).

E_γ	$^{187}Hg^m$ decay		α_K	Theory [31]		Multipolarity	I_i	I_f	E_i	E_f	Note
(keV)	I_γ (ΔI)*	I_e (ΔI)		$E2$	$M1$				(keV)	(keV)	
625.0	12.6(4)	0.08(2)	0.006(2)	E1:	0.0045	E1	$13/2^+$	$11/2^-$	1121.8	496.8	3-m
625.4	2.75(20)	0.036(10)	0.013(4)	0.0118	0.0411	E2	$11/2^+$	$7/2^+$	1121.3	495.6	1-m
629.6	1.1(3)	0.030(4)	0.027(5)	0.0117	0.0404	M1+E2	$11/2^-$	$11/2^-$	1249.4	619.8	3-m
634.9	0.4(1)			0.0115	0.0397		$9/2^-$	$9/2^-$	755.4	120.5	3-m
639.4	8.55(35)	0.22(3)	0.026(3)	0.0113	0.0388	E2+M1	$15/2^-$	$13/2^-$	993.3	353.9	3-m
642.7	1.95(15)	0.04(2)	0.02(1)	0.0112	0.0383	M1+E2	$[17/2^-]$	$15/2^-$	1316.1	673.4	2-m
643.5	0.6(1)	0.021(13)	0.035(20)	0.0112	0.0382	M1(+E2)	$5/2^+$	$5/2^+$	934.5	291.0	1-m
646.3	2.0(2)	0.03(1)	0.014(5)	0.0111	0.0377	(E2)	$11/2^+$	$7/2^+$	1280.8	633.7	1-m
650.9	2.3(2)	0.046(9)	0.020(5)	0.0109	0.0371	E2+M1	$13/2^-$	$11/2^-$	1147.8	496.8	3-m
651.2	0.5(1)	0.020(6)	0.040(16)	0.0109	0.0370	M1	$13/2^-$	$13/2^-$	1393.3	742.1	3-m
653.2	1.75(20)	0.019(5)	0.011(4)	0.0108	0.0367	E2	$11/2^+$	$7/2^+$	1148.8	495.6	1-m
653.9	0.8(2)	0.017(5)	0.021(7)	0.0108	0.0366	M1+E2		$9/2^+$	1420.9	767.0	1-m
657.3	7.0(5)	0.48(7)	0.069(11)	0.0107	0.0361	E0+M1(+E2)	$11/2^-$	$11/2^-$	881.2	223.9	2-m
659.1	0.65(1)	0.008(3)	0.013(6)	0.0106	0.0359	E2(+M1)	$7/2^+$	$9/2^+$	1369.7	710.7	1-m
659.2	0.75(15)	0.029(9)	0.038(13)	0.0106	0.0359	M1	$11/2^-$	$11/2^-$	1156.1	496.8	3-m
659.4	2.4(3)	0.07(2)	0.030(9)	0.0106	0.0358	M1+E2	$9/2^-$	$7/2^-$	984.9	325.9	3-m
667.8	0.9(1)	0.036(10)	0.04(2)	0.0104	0.0347	M1	$5/2^+$	$3/2^+$	687.0	19.5	1-
669.1	3.0(3)	0.03(1)	0.010(6)	0.0103	0.0345	E2	$11/2^+$	$7/2^+$	1164.6	495.6	1-m
669.2	1.05(15)	0.042(19)	0.04(2)	0.0103	0.0345	M1	$13/2^-$	$13/2^-$	1418.2	749.3	2-m
678.9	1.4(3)	0.046(7)	0.033(6)	0.0100	0.0333	M1		$7/2^-$	1276.7	597.8	3-m
683.5	1.3(2)	0.033(6)	0.025(5)	0.0099	0.0327	M1+E2		$9/2^-$	1126.5	443.3	3-m
686.7	0.5(1)	obscured		0.0098	0.0323		$5/2^+$	$1/2^+$	687.0	0.0	1-
692.1	0.3(1)	0.003(2)	0.01(1)	E1:	0.0037	(E1)	$17/2^+$	$17/2^-$	1380.8	689.7	3-m
693.8	1.8(2)	0.04(1)	0.022(6)	0.0096	0.0315	M1+E2	$5/2^+$	$5/2^+$	934.5	240.3	1-m
709.2	1.9(3)	0.04(2)	0.021(11)	0.0092	0.0297	(E2+M1)	$11/2^-$	$9/2^-$	829.3	120.5	3-m
709.9	3.6(3)	0.04(1)	0.012(4)	0.0092	0.0297	E2+(M1)	$9/2^+$	$7/2^+$	1205.5	495.6	1-m
710.3	1.2(1)	0.020(4)	0.017(3)	0.0091	0.0296	M1+E2		$9/2^+$	1420.9	710.7	1-m
712.7	1.45(15)	0.033(8)	0.023(7)	0.0091	0.0294	M1+E2	$11/2^-$	$9/2^-$	1156.1	443.3	3-m
721.7	0.50(15)	0.006(4)	0.012(9)	0.0089	0.0284	(E2)	$11/2^-$	$7/2^-$	1197.6	476.4	2-m
732.1	0.7(1)	0.008(4)	0.011(6)	0.0086	0.0274	(E2)	$19/2^-$	$15/2^-$	1405.2	673.4	2-m
736.3	0.5(1)	0.013(5)	0.026(9)	0.0085	0.0270	M1	$7/2^+$	$7/2^+$	1369.7	633.7	1-m
745.1	1.0(1)	0.018(8)	0.018(9)	0.0083	0.0262	E2+M1	$13/2^-$	$15/2^-$	1418.2	673.4	2-m
747.5	1.55(15)	0.012(3)	0.008(2)	0.0083	0.0260	E2	$(11/2^-)$	$15/2^-$	1420.6	673.4	2-m
751.9	0.6(1)	0.010(4)	0.017(8)	0.0082	0.0256	M1+E2	$9/2^-$	$7/2^-$	1228.8	476.4	2-m
753.1	0.7(2)	0.018(4)	0.026(7)	0.0081	0.0255	M1	$11/2^-$	$11/2^-$	1249.4	496.8	3-m
761.1	0.6(1)	0.002(1)	0.003(2)	E1:	0.0031	(E1)		$11/2^-$	1590.5	829.3	3-m
768.0	3.95(20)	0.012(4)	0.0031(7)	E1:	0.0030	E1	$13/2^+$	$13/2^-$	1121.8	353.9	3-m
773.3	0.7(1)	0.021(5)	0.03(1)	0.0077	0.0238	M1	$13/2^-$	$11/2^-$	1393.3	619.8	3-m
778.8	1.1(1)	0.010(3)	0.009(4)	0.0076	0.0234	(E2)	$7/2^+$	$3/2^+$	1369.7	590.9	1-m
785.3	0.65(15)	0.005(2)	0.008(3)	0.0075	0.0229	E2	$11/2^+$	$7/2^+$	1280.8	495.6	1-m
785.5	0.3(1)	too weak		E1:	0.0029		$13/2^+$	$11/2^-$	1405.5	619.8	3-m
791.3	0.5(1)	0.011(5)	0.022(12)	0.0074	0.0225	M1		$13/2^-$	1540.9	749.3	2-m
795.0	0.8(1)	0.015(3)	0.019(5)	0.0073	0.0221	(M1)	$13/2^-$	$13/2^-$	1147.8	353.9	3-m
805.5	0.95(20)	0.008(3)	0.008(3)	0.0071	0.0215	(E2)	$17/2^-$	$13/2^-$	1158.9	353.9	3-m
805.7	0.65(15)	0.011(3)	0.017(7)	0.0071	0.0215	M1+E2	$11/2^-$	$9/2^-$	1249.4	443.3	3-m
813.3	0.7(1)	0.004(2)	0.006(4)	0.0070	0.0210	E2	$9/2^-$	$5/2^-$	984.9	171.8	3-m
829.9	2.3(2)	0.028(5)	0.012(2)	0.0067	0.0199	M1+E2		$9/2^-$	950.5	120.5	3-m
830.1	0.80(15)	0.006(3)	0.007(4)	0.0067	0.0199	(E2)	$11/2^-$	$7/2^-$	1156.1	325.9	3-m
836.2	3.6(2)	0.024(5)	0.0067(10)	0.0066	0.0195	E2	$13/2^-$	$9/2^-$	956.7	120.5	3-m
840.5	0.75(15)	0.011(3)	0.015(5)	0.0066	0.0193	E2+M1		$13/2^-$	1590.2	749.3	2-m
860.7	1.7(2)	0.017(4)	0.010(2)	0.0063	0.0182	E2	$15/2^-$	$11/2^-$	1357.8	496.8	3-m
864.4	1.2(1)	0.014(3)	0.012(4)	0.0062	0.0180	E2+M1	$9/2^-$	$9/2^-$	984.9	120.5	3-m
867.5	0.45(15)	0.009(3)	0.020(7)	0.0062	0.0178	M1		$15/2^-$	1540.9	673.4	2-m
873.6	1.0(2)	0.020(5)	0.020(6)	0.0061	0.0175	M1	$9/2^-$	$9/2^-$	1317.1	443.3	3-m
895.8	1.65(20)	0.011(3)	0.0066(20)	0.0058	0.0164	E2(+M1)	$11/2^-$	$13/2^-$	1249.4	353.9	3-m

through the $^{187}Hg^g$ decay. The strongest transition in the figure [103.4 keV, $11/2^- \rightarrow 9/2^-$ with $T_{1/2}$=48(2) ns [21]] connects the bandheads of the $h_{11/2}$ and $h_{9/2} \oplus f_{7/2}$ structures. A few transitions with $E1$ multipolarity which connect levels in the $h_{11/2}$ band with levels in the $s_{1/2} \oplus d_{3/2} \oplus d_{5/2}$ structure are also shown. There are no experimentally observed cross-feeding transitions of $E2$ or $M1$ multipolarity between this structure and the $h_{9/2} \oplus f_{7/2}$ band structure.

Figure 9 shows the decay scheme (below 1300 keV) for the level structure of the $h_{9/2} \oplus f_{7/2}$ bands in ^{187}Au observed through the $^{187}Hg^g$ decay. Two transitions with $E0$ components (284.5 and 270.9 keV, $5/2^{-\prime} \rightarrow 5/2^-$ and $1/2^{-\prime} \rightarrow 1/2^-$, respectively) connect the $h_{9/2} \oplus f_{7/2}$ and $(h_{9/2} \oplus f_{7/2})'$ structures. The 101.0 keV transition (with an $E3$

TABLE II. (*Continued*).

E_γ	$^{187}Hg^m$ decay		α_K	Theory [31]		Multipolarity	I_i	I_f	E_i	E_f	Note
(keV)	I_γ (ΔI)*	I_e (ΔI)		$E2$	$M1$				(keV)	(keV)	
896.2	0.65(15)	0.014(4)	0.021(6)	0.0058	0.0164	M1	$13/2^-$	$11/2^-$	1393.3	496.8	3-m
908.5	1.0(1)	obscured		E1:	0.0022		$13/2^+$	$11/2^-$	1405.5	496.8	3-m
914.0	0.8(2)	0.006(2)	0.008(4)	0.0056	0.0156	(E2)	$9/2^+$	$5/2^+$	1205.5	291.0	1-m
951.0	0.65(15)	0.007(2)	0.011(4)	0.0052	0.0141	M1+E2		$7/2^-$	1276.7	325.9	3-m
962.9	1.05(20)	0.006(2)	0.005(2)	0.0051	0.0137	E2	$9/2^-$	$13/2^-$	1317.1	353.9	3-m
963.2	3.55(30)	0.025(6)	0.007(2)	0.0051	0.0137	E2+M1	$13/2^-$	$11/2^-$	1187.0	223.9	2-m
969.7	0.45(15)	0.0015(7)	0.003(2)	E1:	0.0020	(E1)		$11/2^-$	1590.5	619.8	3-m
973.9	1.8(2)	0.018(4)	0.010(2)	0.0050	0.0132	M1+E2	$11/2^-$	$11/2^-$	1197.6	223.9	2-m
1004.2	0.70(15)	0.008(2)	0.011(4)	0.0047	0.0123	M1	$15/2^-$	$13/2^-$	1357.8	353.9	3-m
1014.2	0.65(15)	0.005(2)	0.008(3)	0.0046	0.0120	M1+E2	$15/2^-$	$13/2^-$	1368.1	353.9	3-m
1023.8	0.45(15)	0.0013(6)	0.003(2)	0.0045	0.0117	(E2)	$15/2^-$	$11/2^-$	1905.4	881.2	2-m
1027.3	0.3(1)	too weak					$13/2^-$	$9/2^-$	1147.8	120.5	3-m
1044.1	1.05(15)	0.006(2)	0.0057(20)	0.0043	0.0111	E2+M1		$13/2^-$	1398.0	353.9	3-m
1051.4	0.95(15)	0.003(2)	0.003(2)	E1:	0.0017	(E1)	$13/2^+$	$13/2^-$	1405.5	353.9	3-m
1056.1	0.6(2)	0.0012(6)	0.002(1)	E1:	0.0017	(E1)	$11/2^+$	$11/2^-$	1280.8	223.9	1-m
1058.0	0.5(1)	0.008(3)	0.016(4)	0.0042	0.0108	M1	$15/2^-$	$13/2^-$	1807.6	749.3	2-m
1066.6	2.7(2)	0.015(3)	0.0056(12)	0.0042	0.0106	E2+M1	$15/2^-$	$13/2^-$	1815.9	749.3	2-m
1092.5	0.95(15)	0.007(2)	0.007(2)	0.0040	0.0099	M1+E2	$9/2^-$	$11/2^-$	1317.1	223.9	3-m
1134.0	0.50(15)	0.007(4)	0.015(10)	0.0037	0.0091	M1	$15/2^-$	$15/2^-$	1807.6	673.4	2-m
1142.5	0.8(2)	0.004(2)	0.005(3)	0.0037	0.0089	(E2+M1)	$15/2^-$	$15/2^-$	1815.9	673.4	2-m
1156.9	0.9(2)	0.007(2)	0.008(2)	0.0036	0.0086	M1		$9/2^-$	1276.7	120.5	3-m
1181.2	1.55(15)	0.005(2)	0.003(1)	0.0034	0.0082	E2	$17/2^-$	$13/2^-$	1930.4	749.3	2-m
1181.4	1.8(2)	0.003(2)	0.0017(11)	E1:	0.0014	(E1)	$13/2^+$	$11/2^-$	1405.5	223.9	3-m
1196.6	2.5(2)	0.012(2)	0.005(1)	0.0034	0.0079	E2+M1	$9/2^-$	$9/2^-$	1317.1	120.5	3-m
1232.3	0.5(1)	0.004(2)	0.008(6)	0.0032	0.0074	(M1)	$15/2^-$	$15/2^-$	1905.4	673.4	2-m
1236.6	1.00(15)	0.0018(9)	0.0018(8)	E1:	0.0013	(E1)		$13/2^-$	1590.5	353.9	3-m
1257.0	0.65(15)	0.004(2)	0.006(3)	0.0031	0.0070	(M1+E2)	$17/2^-$	$15/2^-$	1930.4	673.4	2-m
1365.8	2.1(3)	0.0025(8)	0.0012(4)	E1:	0.0011	E1		$11/2^-$	1590.5	223.9	3-m
1583.8	2.0(2)	0.004(1)	0.0019(5)	0.0020	0.0039	E2	$15/2^-$	$11/2^-$	1807.6	223.9	2-m
1592.0	0.4(2)			0.0020	0.0038		$15/2^-$	$11/2^-$	1815.9	223.9	2-m
1681.5	1.35(20)						$15/2^-$	$11/2^-$	1905.4	223.9	2-m

multipolarity and $T_{1/2}$=2.3 s [20]) from the 120.5 keV level connects the $9/2^-$, $h_{9/2}\oplus f_{7/2}$ bandhead, with the $s_{1/2}\oplus d_{3/2}\oplus d_{5/2}$ structure. Bourgeois *et al.* [18] did not establish any of the levels shown in Fig. 9 except the bandhead at 120.6 keV with spin parity of $9/2^-$.

A partial scheme for the decay of $^{187}Hg^m$ is presented in Figs. 10–13. The criteria for its construction are the same as those for the $^{187}Hg^g \rightarrow ^{187}$Au scheme. In total, we have established excited states up to an energy of 2633 keV in ^{187}Au from the $^{187}Hg^m$ β decay. Levels above 1931 keV (60 of them) and their corresponding depopulating transitions (119 of them) are not shown in Figs. 10–13. These can be found in Ref. [25]. Approximately 99% of the total observed decay intensity has been assigned.

The proposed level structure (below 1605 keV) of the $s_{1/2}\oplus d_{3/2}\oplus d_{5/2}$ bands in ^{187}Au, observed through the $^{187}Hg^m$ decay, is shown in Fig. 10. Beside the differences already mentioned in the $^{187}Hg^g$ decay, this scheme is far more complete than that of Bourgeois *et al.* [18], which reported only 15 levels. Additionally, all the levels at and below spin $19/2^+$ seen in the in-beam study [10] are observed in this work.

The proposed level structure (below 1931 keV) of the $h_{11/2}$ bands in ^{187}Au, observed through the $^{187}Hg^m$ decay, is presented in Fig. 11. Two transitions with $E0$ components (657.3 and 437.9 keV, $11/2^{-\prime} \rightarrow 11/2^-$ and $13/2^{-\prime} \rightarrow 13/2^-$, respectively) connect levels of the bands built on the $h_{11/2}$ and $h'_{11/2}$ configurations. The greatest difference between this scheme and that of Bourgeois *et al.* [18] involves an example of coincident pairs of transitions with nearly the same energy: 448.3/525.4 keV and 449.2/524.5 keV. The relative γ-ray intensities of 4.0, 24, 26, and 3.5, respectively, for these transitions, as well as their closeness in energy, is such that they appear as single peaks. Consequently, the only way to separate these pairs is with the running gate method. The results are presented in Fig. 6 where the running gate analysis shows that the association of coincident pairs is 524.5/449.2 between the 1197.6, 673.4, and 223.9 keV levels, and 448.3/525.4 between the 1197.6, 749.3, and 223.9 keV levels. The placement of these four transitions between the 1197.6 and the 223.9 keV levels is only consistent with a spin/parity of $11/2^-$ for the level at 1197.6 keV, rather than $(17/2^-)$ as indicated by Bourgeois *et al.* [18]. These levels are important since they are involved with the lower portion of bands observed by in-beam spectroscopy. In the in-beam data, one study [10] had the band entirely wrong, and the other study [9] had the band partially correct. Another difference between these results and the β-decay data of Bourgeois *et al.* [18] is the spin/parity of the 881 keV level (we have $11/2^-$; they have $13/2^-$). Not only must the 881 keV level be $11/2^-$ from the analysis of the multipolarity of the feeding and depopulating transitions, but the strong $E0$ component in the 657 keV transition demands that it be so. While a careful analysis of the coincidence data reveals its $E0$ char-

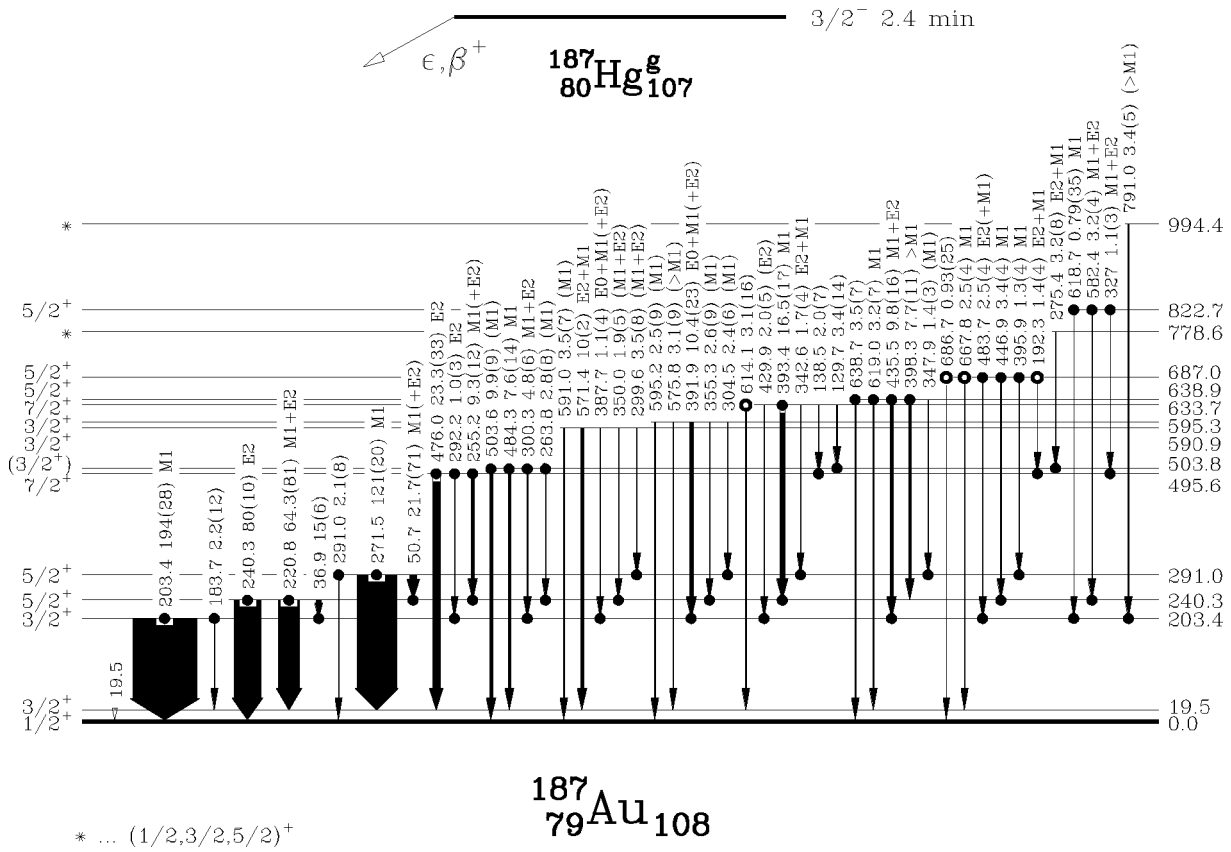

FIG. 7. Proposed level structure of the $s_{1/2}\oplus d_{3/2}\oplus d_{5/2}$ bands in ^{187}Au as a result of the ^{187}Hg^{g} decay. Levels between 0 and 994 keV are shown. The width of the arrow is proportional to the total intensity of a transition. A solid circle indicates a definite coincidence relation while the open circle indicates a weaker one. Transition and level energies are given in keV. Numbers above the arrow are transition energy, total intensity (with the error in last digits in parentheses), and multipolarity of a transition. Levels closer than 11 keV are drawn to be 11 keV apart. An additional 50 transitions and 28 levels, up to 2525 keV, can be found in Ref. [25].

acter [α_K=0.069(11) vs 0.036 for $M1$ (theory)], one can see even in Fig. 1 that one of the transitions at that energy must have a sizable $E0$ component. A difference with the in-beam data of Bourgeois *et al.* [10], for the levels with spin not greater than 19/2, is the spin/parity of the 1316 keV level, which we assign $17/2^-$ rather than $19/2^-$. This assignment is in agreement with the in-beam results of Johansson *et al.* [9].

Figures 12 and 13 show the decay scheme (below 1591 keV) for the proposed level structure of the $h_{9/2}\oplus f_{7/2}$ and $i_{13/2}$ bands in ^{187}Au observed through the ^{187}Hg^{m} decay. Three out of five transitions with $E0$ components observed in the $h_{9/2}\oplus f_{7/2}$ structure (322.9, 388.2, and 478.1 keV, $9/2^{-\prime}\rightarrow 9/2^-$, $13/2^{-\prime}\rightarrow 13/2^-$, and $17/2^{-\prime}\rightarrow 17/2^-$, respectively) are associated with the ^{187}Hg^{m} decay. These transitions connect levels of the bands built on the $h_{9/2}\oplus f_{7/2}$ and $(h_{9/2}\oplus f_{7/2})'$ configurations. Transitions with $E1$ multipolarity (768.0, 625.0, 501.9, 305.4, and 292.1 keV) connect the $i_{13/2}$ bandhead at 1121.8 keV to levels of the $h_{9/2}\oplus f_{7/2}$ structure. The next $i_{13/2}$ band member ($17/2^+$ at 1380.8 keV) is connected to the $h_{9/2}\oplus f_{7/2}$ structure through $E1$ transitions (692.1, 564.8, and 387.5 keV) and to the $i_{13/2}$ bandhead through an $E2$ transition of 259.2 keV. The in-beam work of Bourgeois *et al.* [10] gives two possible spin values for the band which they label #5. This is the structure that corresponds to our excited band built on the $9/2'$ level. They [10] base their spin/parity assignments on ''the character of the highly-converted transitions between band #5 and band #1 being M1 with an anomaly in the conversion coefficient.'' Through analysis of the feeding and depopulating transitions our work confirms the spin/parity assignments reported in the work of Zganjar *et al.* [32]. Among interband transitions there are five $E0$-enhanced transitions, not anomalous $M1$ transitions as Bourgeois *et al.* [18] reported. These $E0$-enhanced transitions demand the spin/parity sequence as reported in our scheme, which actually agrees with the higher values of the spin/parity reported in the in-beam data of Bourgeois *et al.* [10].

Separated schemes of ^{187}Hg^{g} and ^{187}Hg^{m} decays reveal quite different parts of the ^{187}Au structure. The 203.4 keV transition is the strongest in the ^{187}Hg^{g} ($J^\pi=3/2^-$) decay, while the 233.4 keV transition is the strongest in the ^{187}Hg^{m} ($J^\pi=13/2^+$) decay. The decay of the ^{187}Hg $3/2^-$ ground state reveals 62 mostly low-spin levels in ^{187}Au, connected by 171 transitions. The decay of the ^{187}Hg $13/2^+$ isomer reveals 148 mostly high-spin levels in ^{187}Au, connected by 362 transitions. Out of these, 16 levels and 42 transitions are common to both decays. Different aspects of the ^{187}Au structure, revealed by the separated $3/2^-$ or $13/2^+$ decays, can be seen in Fig. 3 where a portion of the spectrum from each decay is shown with the same gate. In general, transitions that depopulate low-spin levels (such as 392 and 579 keV) are stronger in the upper section of each gate, while transitions that depopulate high-spin levels (such as 470 and 363 keV) are stronger in the lower section.

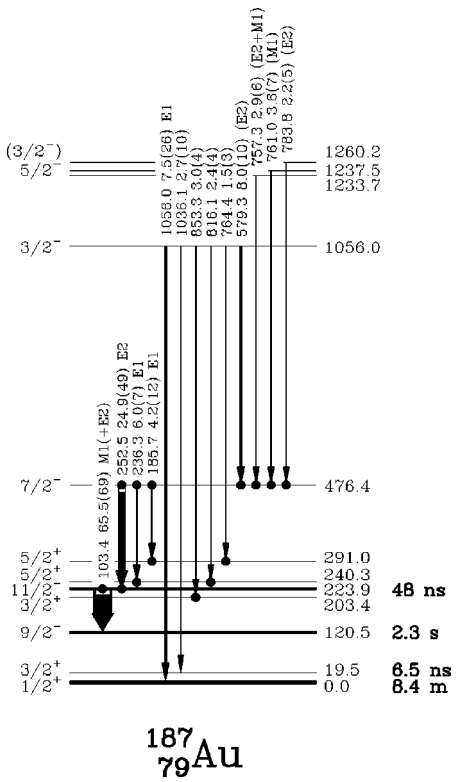

FIG. 8. Proposed level structure of the $h_{11/2}$ bands in ^{187}Au as a result of the ^{187}Hg^{g} decay. Levels between 0 and 1260 keV are shown. An additional three transitions and three levels, up to 2179 keV, can be found in Ref. [25]. See caption to Fig. 7 for details.

Data such as that presented here for the decay of ^{187}Hg^{m,g} to levels in ^{187}Au can play a unique role in determining the low-spin structure, especially the parity, of bands observed by in-beam spectroscopy where only the yrast states receive appreciable population. We present, in Figs. 14 and 15, the parts of the structure based on $\pi^{+1}(h_{9/2}\oplus f_{7/2})$, $\pi^{-1}h_{11/2}$, and $\pi^{-1}(s_{1/2}\oplus d_{3/2}\oplus d_{5/2})$, which are common to both the in-beam data and the data obtained here by radioactive decay of ^{187}Hg^{m,g}. Our relative transition intensities, as well as level energies and spin/parity assignments, are drawn in the form used in the in-beam data, for easier comparison. The two values for the possible spin assignments for the part of the structure assigned as band #5 in [10] are uniquely defined in our $\pi^{+1}(h_{9/2}\oplus f_{7/2})$ decay scheme (the leftmost series of levels and transitions in Fig. 14). The rest of the structure presented in Fig. 14 shows our analog of the remaining parts of the in-beam data [9,10] for this configuration.

The upper part of Fig. 15 shows the band structure built upon the $\pi^{-1}h_{11/2}$ configuration and the lower part of the figure shows the band structure built upon the $\pi^{-1}(s_{1/2}\oplus d_{3/2}\oplus d_{5/2})$ configuration, which are common to our results and those of the in-beam data [9,10]. Our $\pi^{-1}h_{11/2}$ structure differs on a few points with the in-beam data [10], in that the strong 449.2 and 525.4 keV transitions and the weaker 448.3 and 524.5 keV transitions have been properly assigned in this work as a result of the running gate analysis. The $\pi^{-1}(s_{1/2}\oplus d_{3/2}\oplus d_{5/2})$ level structure presented in Fig. 15 shows that the low-spin part of the in-beam data [10] for this configuration has been correctly defined.

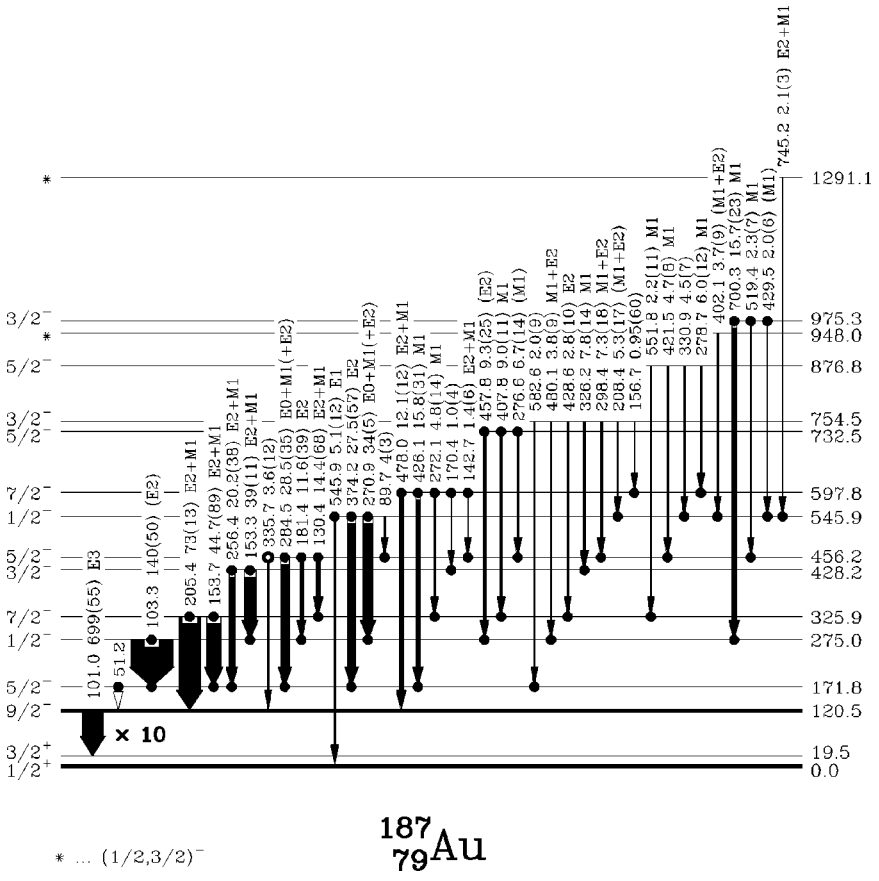

FIG. 9. Proposed level structure of the $h_{9/2}\oplus f_{7/2}$ bands in ^{187}Au as a result of the ^{187}Hg^{g} decay. Levels between 0 and 1291 keV are shown. The actual total intensity of the 101.0 keV transition is 10 times the width drawn. The intensity of the 51.2 keV transition in the low-spin structure could not be found using gated spectra, and so the transition is drawn without width (white arrow). An additional 23 transitions and 11 levels, up to 2323 keV, can be found in Ref. [25]. See caption to Fig. 7 for details.

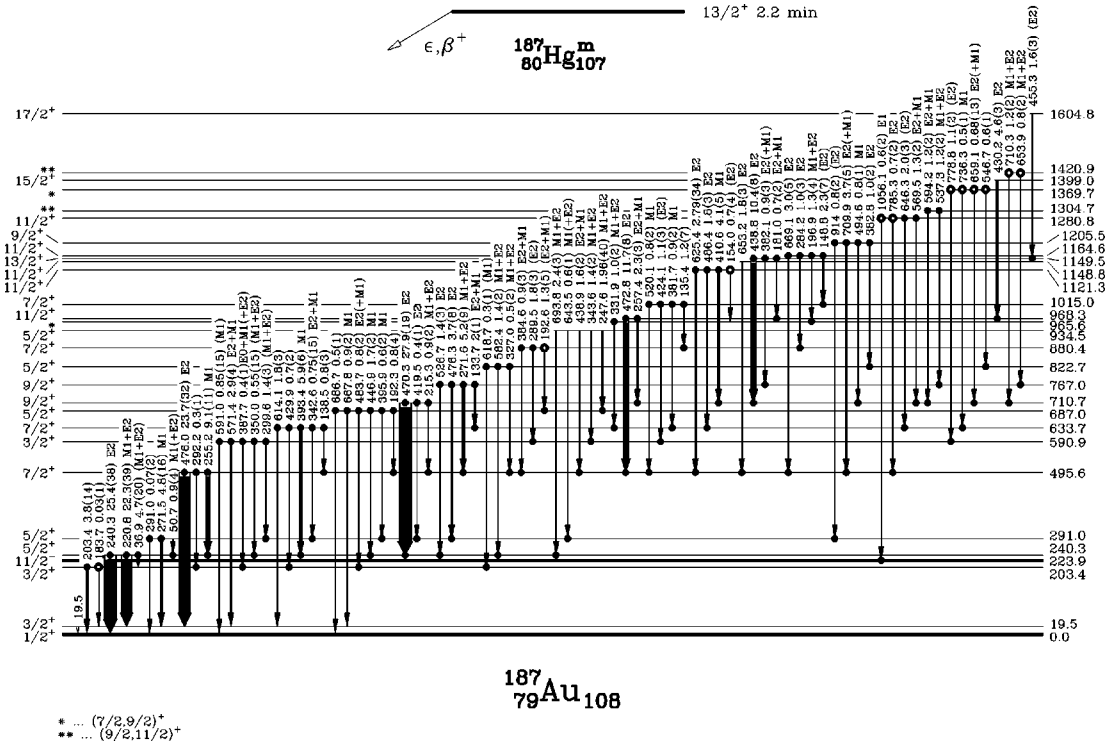

FIG. 10. Proposed level structure of the $s_{1/2} \oplus d_{3/2} \oplus d_{5/2}$ bands in ^{187}Au as a result of the ^{187}Hg^{m} decay. Levels between 0 and 1605 keV are shown. An additional 26 transitions and 13 levels, up to 2346 keV, can be found in Ref. [25]. See caption to Fig. 7 for details.

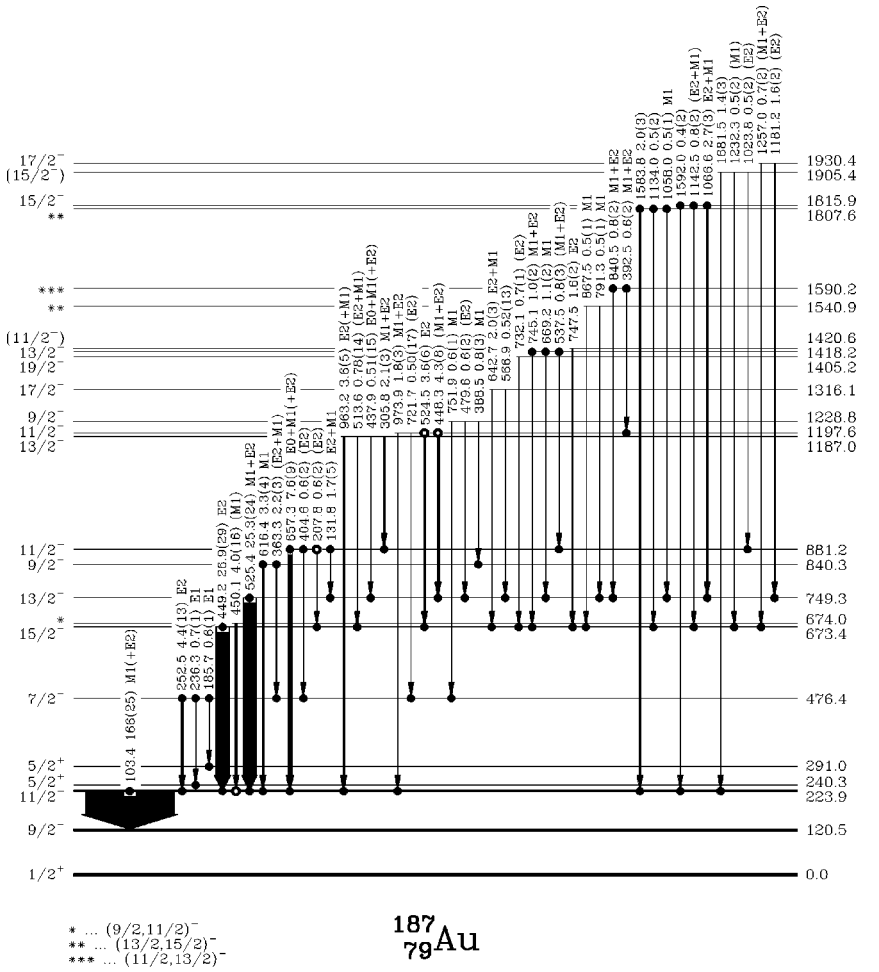

FIG. 11. Proposed level structure of the $h_{11/2}$ bands in ^{187}Au as a result of the ^{187}Hg^{m} decay. Levels between 0 and 1418 keV are shown. An additional 32 transitions and 19 levels, up to 2625 keV, can be found in Ref. [25]. See caption to Fig. 7 for details.

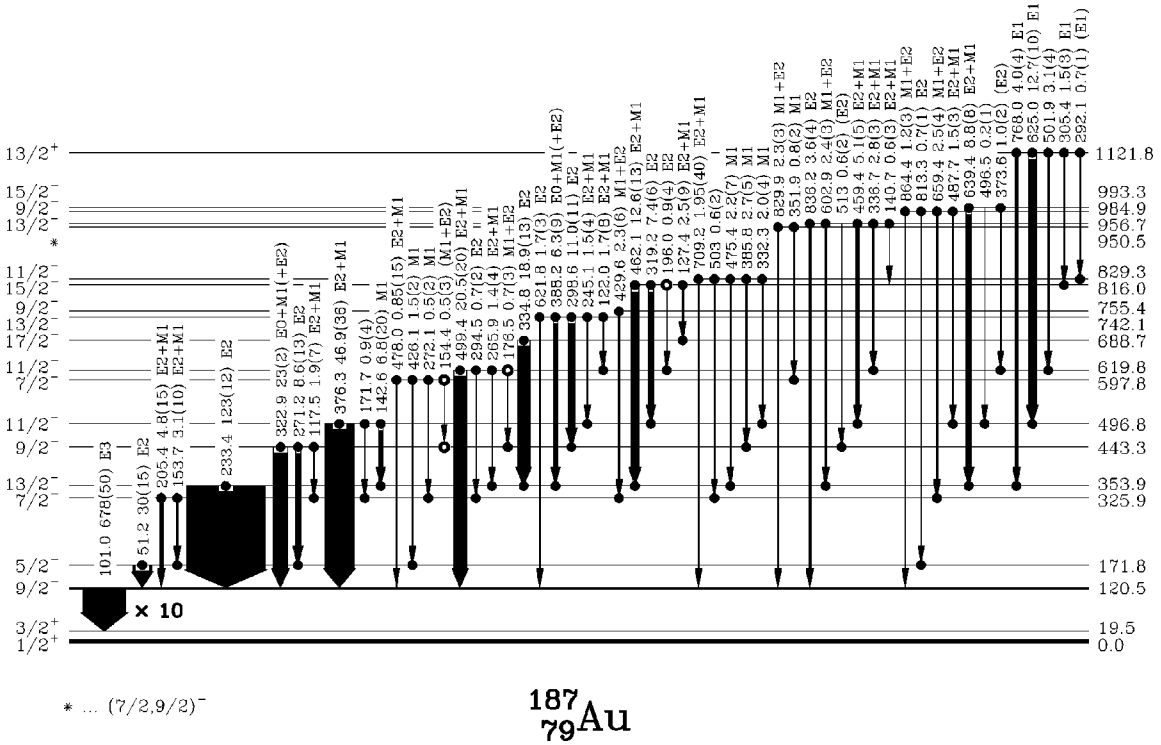

FIG. 12. Proposed level structure of the $h_{9/2} \oplus f_{7/2}$ bands in ^{187}Au as a result of the ^{187}Hg^m decay. Levels between 0 and 1127 keV are shown. The total intensity of the 101.0 keV transition is 10 times the width drawn. See caption to Fig. 7 for details.

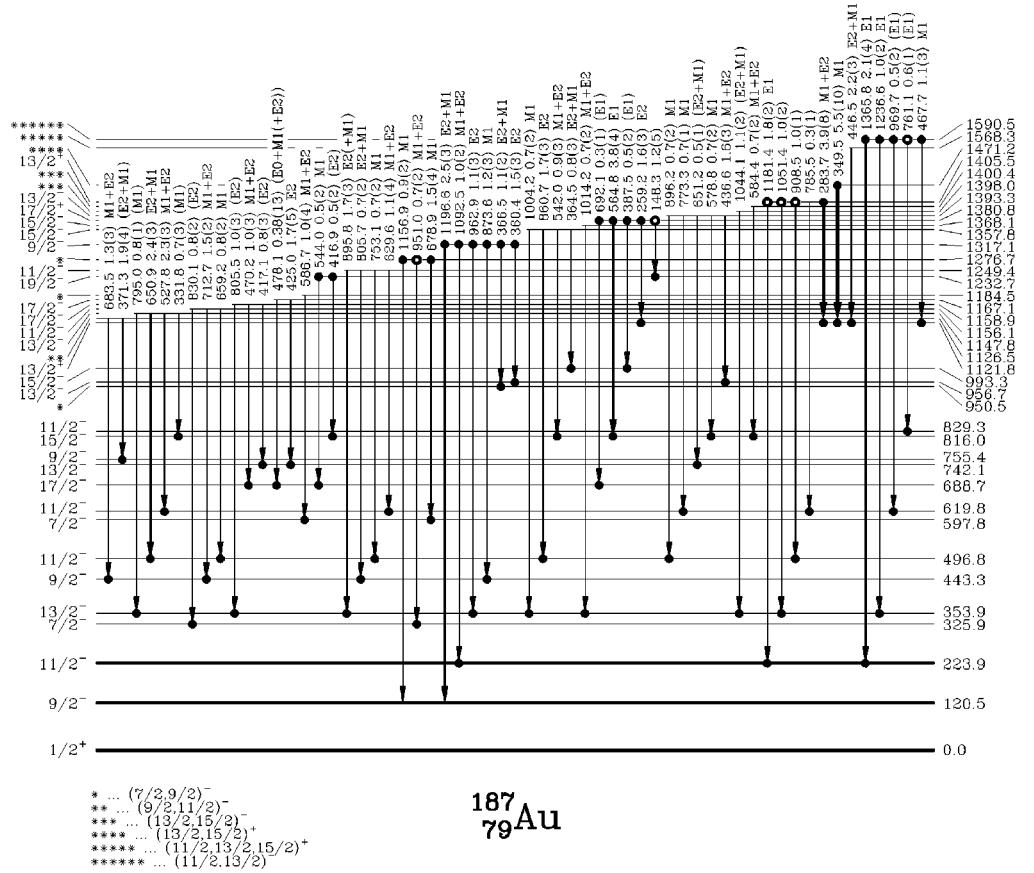

FIG. 13. Proposed level structure of the $h_{9/2} \oplus f_{7/2}$ bands in ^{187}Au as a result of the ^{187}Hg^m decay. Levels between 0 and 1591 keV are shown. Additional 60 transitions and 28 levels, up to 2633 keV, can be found in Ref. [25]. See caption to Fig. 7 for details.

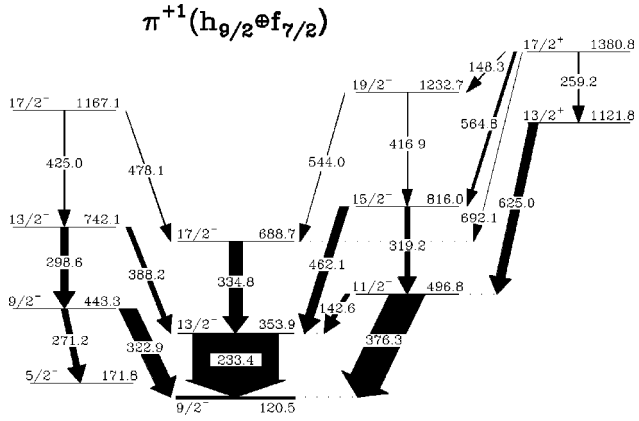

FIG. 14. A part of the $\pi^{+1}(h_{9/2}\oplus f_{7/2})$ structure in ^{187}Au that corresponds to the lower-spin part of the in-beam data [10,9].

V. DISCUSSION AND COMPARISON WITH THEORY

A major goal of the present work is to locate and characterize, as completely as possible, new low-energy collective structures that intrude into the systematic patterns of states established in heavier neighboring nuclei. Our recent study [4] of ^{189}Au summarizes these systematic patterns and provides an extensive base for comparison with the present results. The following discussion is a natural continuation of the previous work and additional details and references can be found there [4].

Calculations have been performed with the particle + triaxial rotor model (PTRM) [33] using a Woods-Saxon potential for the deformed mean field. The same potential has also been used to describe the neighboring even-even Pt and Hg nuclei [34] as well as single-proton bandheads in this region

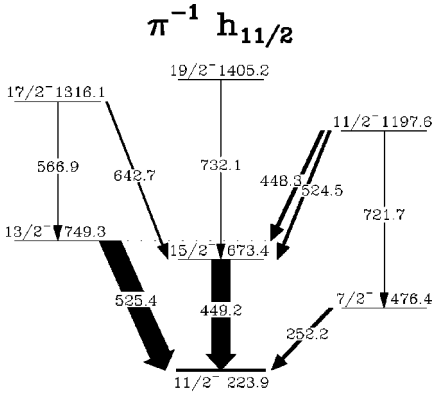

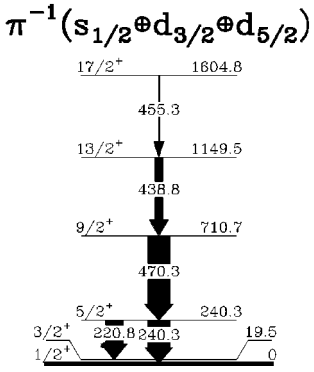

FIG. 15. Top: a part of the $\pi^{-1}h_{11/2}$ structure in ^{187}Au that corresponds to the lower-spin part of the in-beam data [10,9]. A few differences are explained in the text. Bottom: a part of the $\pi^{-1}(s_{1/2}\oplus d_{3/2}\oplus d_{5/2})$ structure that corresponds to the lower-spin part of the in-beam data [10] and agrees with it.

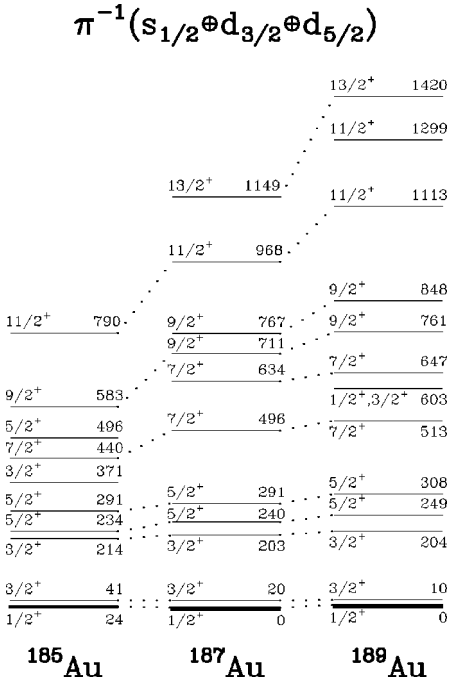

FIG. 16. Systematics of the $\pi^{-1}(s_{1/2}\oplus d_{3/2}\oplus d_{5/2})$ states in the ^{185}Au, ^{187}Au, and ^{189}Au isotopes. The levels are drawn so that the first $3/2^+$ level in each nucleus is at the same position.

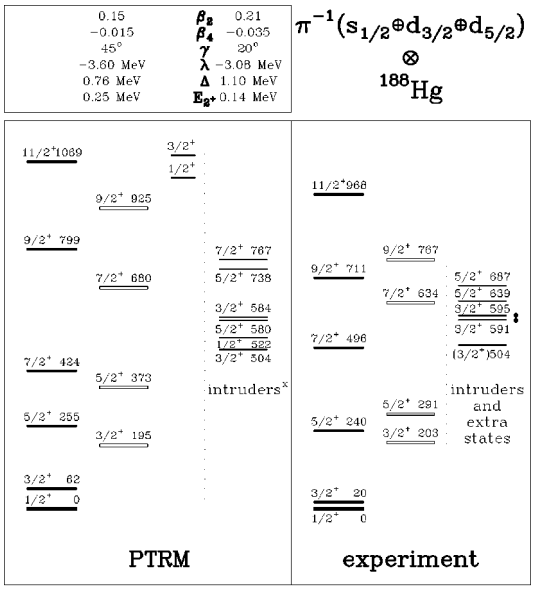

[x] the calculated band head energy is adjusted to the valeu of 504 keV

FIG. 17. The $s_{1/2}\oplus d_{3/2}\oplus d_{5/2}$ and $(s_{1/2}\oplus d_{3/2}\oplus d_{5/2})'$ (denoted as ''intruders'') family of positive-parity states in ^{187}Au (separated by a dotted line). The left part of the figure shows the results of the PTRM calculations, and the right part shows the experimental data. Level energies are given in keV relative to the basic state. The bandhead energy for the calculated intruder band is adjusted to be the same as the experimental bandhead energy. λ is the Fermi energy, Δ is the pairing gap, and E_{2^+} is the energy of the 2^+ level in the chosen core nucleus, all given in MeV. Levels depopulated by $E0$ transitions are denoted by a solid circle.

TABLE III. List of experimental and calculated relative γ-ray intensities for a few low-lying levels in the $s_{1/2}\oplus d_{3/2}\oplus d_{5/2}$ bands of ^{187}Au. An asterisk indicates experiment only, $I_{\rm tot}$, a dagger indicates to see the text in reference to weak transitions.

Relative I_γ			
Position	Eγ (keV)	PTRM calc.	experiment
$3/2_2^+ \rightarrow 1/2_1^+$	203.4	100	100
$3/2_2^+ \rightarrow 3/2_1^+$	183.7	4	1.4(6)†
$5/2_1^+ \rightarrow 1/2_1^+$	240.3	100	100
$5/2_1^+ \rightarrow 3/2_1^+$	220.8	361	72(7)
$5/2_1^+ \rightarrow 3/2_2^+$	36.9*	<1	
$5/2_2^+ \rightarrow 1/2_1^+$	291.0	3	2.3(8)†
$5/2_2^+ \rightarrow 3/2_1^+$	271.5	100	100
$5/2_2^+ \rightarrow 3/2_2^+$	88	1	
$5/2_2^+ \rightarrow 5/2_1^+$	50.7*	<1	
$7/2_1^+ \rightarrow 3/2_1^+$	476.0	100	100
$7/2_1^+ \rightarrow 3/2_2^+$	292.2	<1	4(1)†
$7/2_1^+ \rightarrow 5/2_1^+$	255.2	1	28(3)
$7/2_1^+ \rightarrow 5/2_2^+$	205	1	
$7/2_2^+ \rightarrow 3/2_1^+$	614.1	6	21(10)
$7/2_2^+ \rightarrow 3/2_2^+$	429.9	12	13(2)
$7/2_2^+ \rightarrow 5/2_1^+$	393.4	100	100
$7/2_2^+ \rightarrow 5/2_2^+$	342.6	7	11(2)
$7/2_2^+ \rightarrow 7/2_1^+$	138.5	<1	3(1)
$9/2_1^+ \rightarrow 5/2_1^+$	470.3	100	100
$9/2_1^+ \rightarrow 5/2_2^+$	419.5	<1	1.5(4)
$9/2_1^+ \rightarrow 7/2_1^+$	215.3	1	2.2(4)
$9/2_1^+ \rightarrow 7/2_2^+$	77	<1	
$9/2_2^+ \rightarrow 5/2_1^+$	526.7	<1	45(7)
$9/2_2^+ \rightarrow 5/2_2^+$	476.3	88	86(14)
$9/2_2^+ \rightarrow 7/2_1^+$	271.6	100	100
$9/2_2^+ \rightarrow 7/2_2^+$	133.7	4	17(7)
$9/2_2^+ \rightarrow 9/2_1^+$	56	<1	

[35]. For each set of calculations discussed below, the β_2 and β_4 deformation parameters are taken from the bandhead predictions [35] or the even-even neighbors [34]. The triaxiality parameter γ is fitted to the experimental data. The core 2^+ energy is estimated using Grodzins' rule, but adjusted slightly to the data. Pairing is treated within the BCS method, so that the Fermi energy (λ) and pairing gap (Δ) are derived and not input parameters. The PTRM Hamiltonian is diagonalized within the space of low-lying one-quasiparticle states. Magnetic dipole matrix elements are calculated with the core g factor (g_R) estimated as Z/A and the spin g factor for the odd proton (g_s) taken as 70% of the free

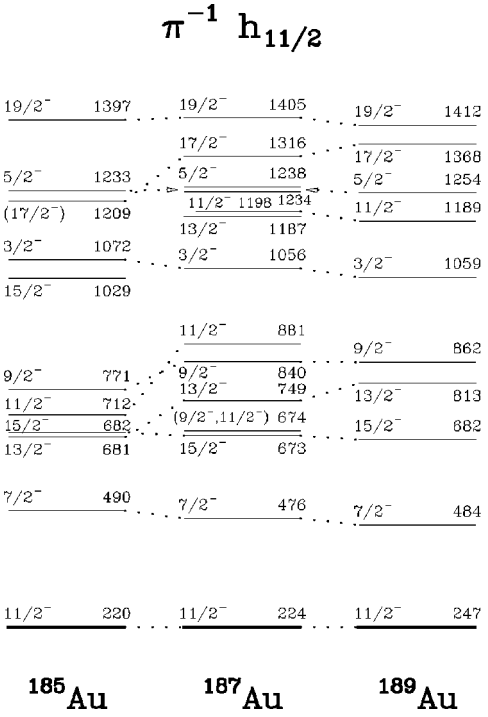

FIG. 18. Systematics of the $\pi^{-1}(h_{11/2})$ states in the ^{185}Au, ^{187}Au, and ^{189}Au isotopes. The levels are drawn so that the first $11/2^-$ level in each nucleus is at the same position.

value. The experimental states have been grouped into four distinct structures, the $s_{1/2}\oplus d_{3/2}\oplus d_{5/2}$, the $h_{11/2}$, the $h_{9/2}\oplus f_{7/2}$, and the $i_{13/2}$ bands.

In the present version of the PTRM, the core is restricted to a fixed shape and all energies are computed relative to the BCS vacuum state at that deformation. Consequently, *when calculations are made for different core shapes, no mixing is included between the coexisting shapes, and the energy difference between coexisting states is not calculated.*

A. Positive-parity $\pi^{-1}(s_{1/2}\oplus d_{3/2}\oplus d_{5/2})$ structure

A prominent feature of the low-lying positive-parity states in $^{185-195}$Au is the occurrence of two rotational bands built on $1/2^+$ and $3/2^+$ bandheads. These two bands are remarkably similar throughout the sequence $^{189-195}$Au, but are clearly more compressed in ^{185}Au and ^{187}Au than in ^{189}Au, as shown in Fig. 16. PTRM calculations for ^{187}Au are compared with the experimental data in Fig. 17. The calculated energy levels to the left of the dotted line are obtained for a deformation of $\beta_2=0.15$ and $\gamma=45°$, and the agreement with the two main rotational bands is satisfactory. Calculated and experimental relative γ-ray intensities are compared in Table III, and again the agreement is satisfactory. The measured magnetic moment for the ground state, $\mu(1/2^+)=+0.53\ \mu_N$ [30], and values for the $B(E2;\ 3/2_1^+\rightarrow 1/2_1^+)=0.18\ e^2\,b^2$ and $B(M1:\ 3/2_1^+\rightarrow 1/2_1^+)=(4.8\times 10^{-4})\ \mu_N{}^2$ [22] are also well described; the corresponding calculated values are $+0.54\mu_N$, $0.21\ e^2\,b^2$, and $B(M1)<10^{-4}\ \mu_N{}^2$, respectively. As noted previously for ^{189}Au [4], the calculated magnetic moment is particularly sensitive to the triaxiality γ. This core shape is essentially the same weakly deformed, slightly triaxial, ''ob-

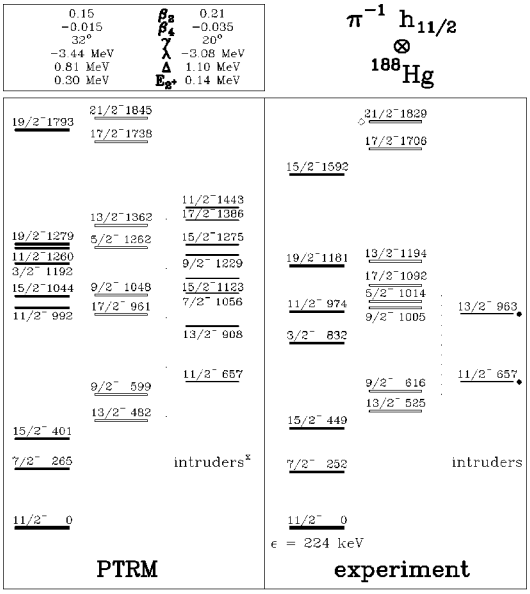

FIG. 19. The $h_{11/2}$ and $(h_{11/2})'$ (denoted as ''intruders'') family of negative-parity states in ^{187}Au (separated by a dotted line). The left part of the figure shows the results of the PTRM calculation, while on the right are experimental data. Level energies are given in keV relative to the lowest state in the family. The bandhead energy for the calculated intruder band is adjusted to be the same as the experimental bandhead. For the defintions of λ, Δ, and E_{2^+}, see Fig. 17. Levels depopulated with $E0$ transitions are denoted by a solid circle. An open diamond denotes a level seen in the experimental in-beam data [10,9].

latish'' shape that successfully described the positive-parity states in ^{189}Au. Furthermore, the experimental electromagnetic data [the relative γ-ray intensities, the magnetic moment, and the $B(E2)$ and $B(M1)$ values] are very similar for ^{187} Au and ^{189}Au, and the level of agreement with the calculations is nearly identical in the two cases. This extensive agreement strongly supports the deformation used for these low-lying states.

However, one interesting disagreement remains: The compression of these positive-parity bands compared to ^{189}Au apparently cannot be explained as a deformation effect, and is only modeled in the PTRM calculations by adjusting the core 2^+ energy, but is not explained. One possibility is that some mixing with the higher-lying intruder states compresses these bands, but it is not strong enough to destroy the similarities of the electromagnetic properties between ^{187}Au and ^{189}Au.

An interesting feature of the experimental electromagnetic data seen in all three isotopes ^{185}Au [5,26], ^{187}Au, and ^{189}Au [4] is a series of weak transitions between the $3/2_2^+$ and $3/2_1^+$, $5/2_2^+$ and $1/2_1^+$, and $7/2_1^+$ and $3/2_2^+$ levels. The experimental and PTRM γ-ray intensities for these transitions in ^{187}Au are noted in Table III. The branching ratios obtained from the PTRM calculations are in qualitative agreement with the experimental values for these cases.

The ''oblate''calculations for the $s_{1/2}\oplus d_{3/2}\oplus d_{5/2}$ structure cannot account for the ''extra'' positive-parity states found experimentally, beginning with the level at 504 keV (denoted as ''intruders'' in the experimental part of Fig. 17). The transitions with enhanced $E0$ components (at 387.7 and 391.9 keV) that decay to the $s_{1/2}\oplus d_{3/2}\oplus d_{5/2}$ band also indicate that this group of states has a different structure. A separate PTRM calculation was made with deformation parameters that gave the best description of the $h_{9/2}\oplus f_{7/2}$ bands (discussed below); this deformation is very similar to that

TABLE IV. Calculated and experimental relative γ-ray intensities for the $h_{11/2}$ band of ^{187}Au.

Relative I_γ			
Position	E_γ (keV)	PTRM calc.	experiment
$9/2_1^-\rightarrow 11/2_1^-$	616.4	100	100
$9/2_1^-\rightarrow 7/2_1^-$	363.3	139	67.7(9)
$11/2_2^-\rightarrow 11/2_1^-$	973.9	108	45(7)
$11/2_2^-\rightarrow 7/2_1^-$	721.7	92	12.5(4)
$11/2_2^-\rightarrow 15/2_1^-$	524.5	2	87.5(15)
$11/2_2^-\rightarrow 13/2_1^-$	448.3	100	100
$11/2_2^-\rightarrow 9/2_1^-$	357	384	
$11/2_2^-\rightarrow 11/2_1^-$	973.9	170	45(7)
$11/2_2^-\rightarrow 7/2_1^-$	721.7	2	12.5(4)
$11/2_2^-\rightarrow 15/2_1^-$	524.5	1	87.5(15)
$11/2_2^-\rightarrow 13/2_1^-$	448.3	100	100
$11/2_2^-\rightarrow 9/2_1^-$	357	1	
$9/2_2^-\rightarrow 11/2_1^-$	1005	100	
$9/2_2^-\rightarrow 7/2_1^-$	751.9	1	86(20)
$9/2_2^-\rightarrow 13/2_1^-$	479.6	<1	79(20)
$9/2_2^-\rightarrow 9/2_1^-$	388.5	<1	100
$5/2_1^-\rightarrow 7/2_1^-$	761.0	100	100(14)
$5/2_1^-\rightarrow 9/2_1^-$	398	<1	
$5/2_1^-\rightarrow 3/2_1^-$	182	3	
$17/2_1^-\rightarrow 15/2_1^-$	642.7	100	100
$17/2_1^-\rightarrow 13/2_1^-$	566.9	11	25.6(55)
$13/2_2^-\rightarrow 11/2_1^-$	1194	50	
$13/2_2^-\rightarrow 15/2_1^-$	745.1	1316	95(17)
$13/2_2^-\rightarrow 13/2_1^-$	669.2	100	100
$13/2_2^-\rightarrow 9/2_1^-$	578	27	
$13/2_2^-\rightarrow 11/2_2^-$	221	41	
$15/2_2^-\rightarrow 11/2_1^-$	1592.0	16	14.8(75)
$15/2_2^-\rightarrow 15/2_1^-$	1142.5	6	29.6(77)
$15/2_2^-\rightarrow 13/2_1^-$	1066.6	100	100
$15/2_2^-\rightarrow 11/2_2^-$	618	1	
$15/2_2^-\rightarrow 17/2_1^-$	500	2	
$17/2_2^-\rightarrow 15/2_1^-$	1257.0	5	42(10)
$17/2_2^-\rightarrow 13/2_1^-$	1181.3	100	100
$17/2_2^-\rightarrow 17/2_1^-$	614	16	
$17/2_2^-\rightarrow 19/2_1^-$	515	28	
$17/2_2^-\rightarrow 13/2_2^-$	512	4	

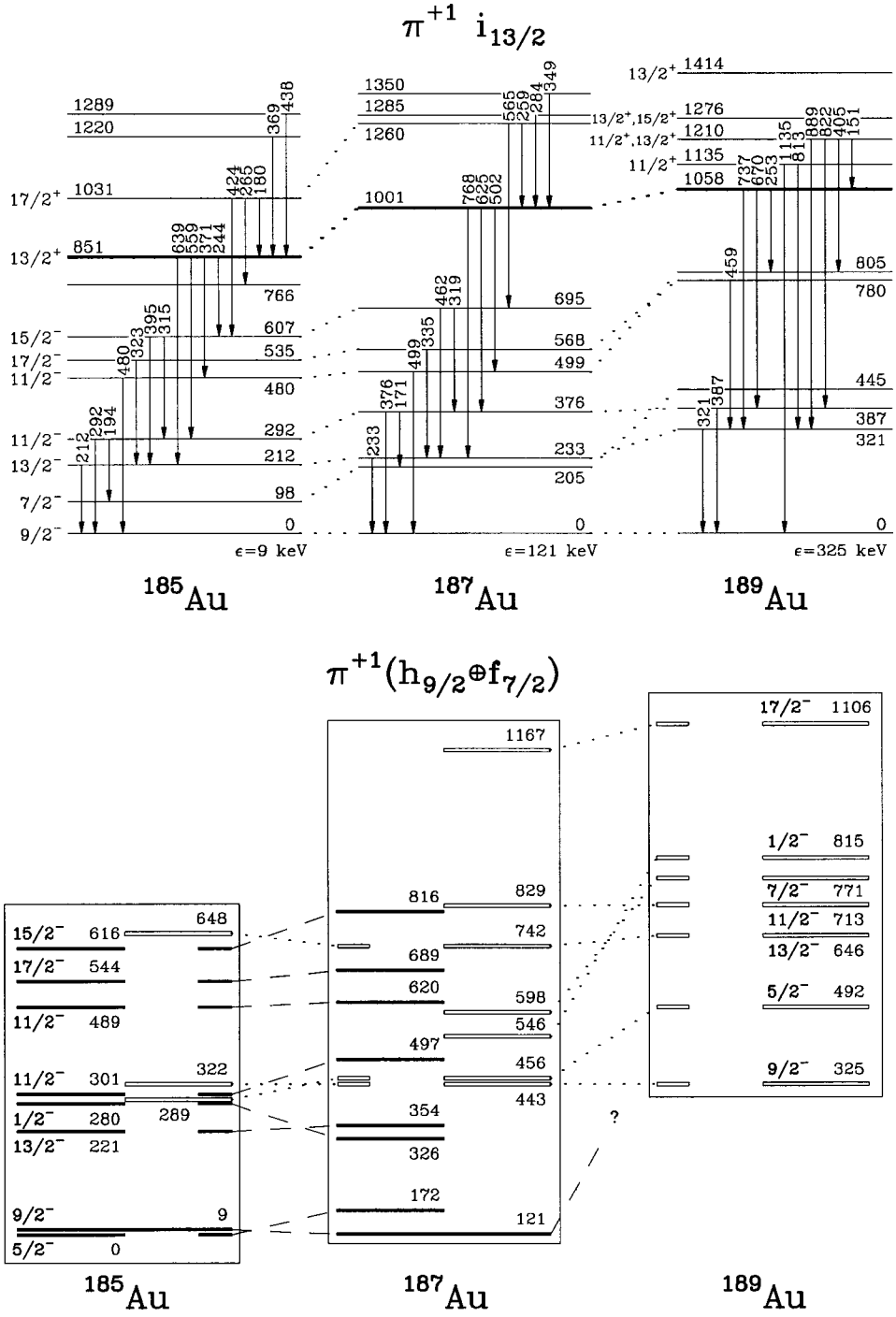

FIG. 20. Systematics of the $\pi^{+1}(i_{13/2})$ states are drawn in the top part of the upper figure. Transitions that connect $i_{13/2}$ to the $h_{9/2}\oplus f_{7/2}$ structure are shown. The bottom part of the figure is the structure of the $\pi^{+1}(h_{9/2}\oplus f_{7/2})$ states in the ^{185}Au, ^{187}Au, and ^{185}Au isotopes.

expected for the prolate structures in ^{186}Pt and ^{188}Hg [34]. The energy of the calculated intruder bandhead was adjusted to be the same as the experimental bandhead, but the relative energies of the other calculated states are correctly shown.

The experimental level density and spin assignments agree qualitatively with the calculated $(s_{1/2}\oplus d_{3/2}\oplus d_{5/2})'$ structure, although one calculated $1/2^+$ state has no experimental counterpart and there are only two calculated $3/2^+$ states, but three experimental $3/2^+$ states. If these intruder states are well-deformed structures, then there should exist associated rotational bands. Observing those associated states and their decay properties would help to elucidate the structure of these intruder levels, although we note that at the low spins seen in this work, mixing is certainly obscuring any clear band pattern.

B. Negative-parity $\pi^{-1}h_{11/2}$ structure

The level energies of the $\pi^{-1}h_{11/2}$ structures in ^{185,187,189}Au are very similar to each other, as shown in Fig. 18. PTRM calculations are compared with the experimental data in Fig. 19, where calculated states to the left of the dotted line are based on a weakly deformed triaxial shape ($\beta_2=0.15$, $\gamma=32°$). The triaxiality parameter γ has been fitted to the splitting of the $15/2^-$ and $13/2^-$ states, and in the figure the $I=11/2\pm 2n$ states are separated from the $I=11/2\pm(2n+1)$ states. Overall, there is good agreement between the experimental and calculated energy spectra, and every calculated state up to $\sim$1 MeV, above the $11/2^-$ bandhead, has an experimental counterpart. A comparison of calculated and experimental relative γ-ray intensities for the

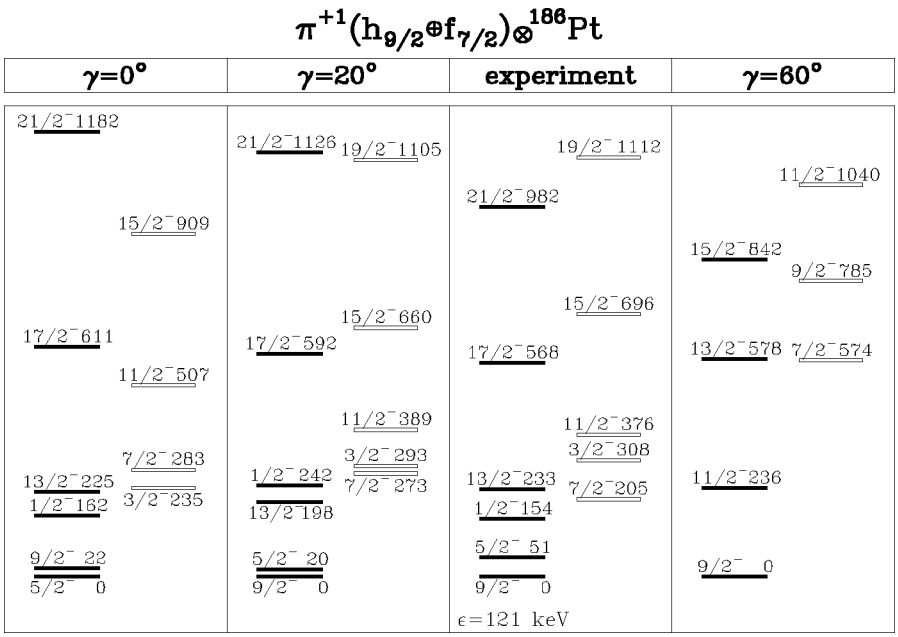

FIG. 21. The $h_{9/2}\oplus f_{7/2}$ structure as a result of the PTRM calculations for three different values of γ (0°, 20°, and 60°) and the experimental levels. The oblate shape structure $\gamma=60°$ differs with the experimental levels the most, while the best agreement is achieved for the prolate shape structure with $\gamma=20°$.

$h_{11/2}$ structure is presented in Table IV, and the agreement is reasonably good although some clear discrepancies exist. The first ''$11/2_2$'' listed in the table uses the second calculated $11/2^-$ state, while the second ''$11/2_2$'' listed in the table uses the third calculated $11/2^-$ state. Clearly neither of the calculated $11/2^-$ states describes the experimental pattern of relative γ-ray intensities very well, although some difficulties were also noted for the second and third $11/2^-$ states in ^{189}Au [4]. Some discrepancies are also apparent for the second calculated $9/2^-$ state, but no comparison with ^{189}Au is available for this state. Overall, the agreement between these PTRM calculations and the data is comparable to the agreement found in ^{189}Au [4].

The $h_{11/2}$ intruder levels are shown to the right of the dotted lines in Fig. 19. Note that the two experimental levels, with spins $11/2^-$ and $13/2^-$, have $E0$ transitions to members of the weakly deformed $h_{11/2}$ structure. The calculated levels use the same triaxial shape ($\beta_2=0.21$, $\gamma=20°$) as used for the $h_{9/2}\oplus f_{7/2}$ bands. The calculated $11/2^-$ and $13/2^-$ states are the first two members of a strongly coupled band built on the [505]$11/2^-$ Nilsson orbital, and the calculated $7/2^-$ and $15/2^-$ states are rotational bandheads with $K=11/2\pm2$ that come low in energy due to the moderate triaxiality. If the observed $11/2^-$ and $13/2^-$ states are indeed part of the [505]$11/2^-$ band, there should be additional band members above these. Also, the existence of such low-lying $7/2^-$ and $15/2^-$ intruder bandheads would be a strong indication of triaxiality (or some γ softness).

C. Negative-parity $\pi^{+1}(h_{9/2}\oplus f_{7/2})$ and positive-parity $\pi^{+1}i_{13/2}$ structures

The systematic pattern of states associated with the $\pi^{+1}(h_{9/2}\oplus f_{7/2})$ and $\pi^{+1}i_{13/2}$ configurations in ^{185,187,189}Au is shown in Fig. 20. In the upper portion of the figure, the $i_{13/2}$ energy levels and the connecting transitions to the negative-parity states are shown, all drawn relative to the lowest $9/2^-$ state. A more complete listing of the $h_{9/2}\oplus f_{7/2}$ states in ^{187}Au and their suggested analog in ^{185,189}Au is shown in the lower portion of the figure. One striking feature of these systematics is the much larger number of states found at low energy in ^{185,187}Au than in ^{189}Au. Our recent study of ^{189}Au [4] showed that the experimental data are probably complete to an excitation energy of at least $\sim$812 keV, and furthermore, there is a one-to-one correspondence between the $h_{9/2}\oplus f_{7/2}$ states observed in ^{189}Au and those calculated with the PTRM within $\sim$900 keV of the bandhead. The appearance of these ''extra'' states along with the observed $E0$ transitions clearly indicates coexisting sets of $h_{9/2}\oplus f_{7/2}$ states at low energy in ^{187}Au.

PTRM calculations for a variety of triaxialities are compared with the two lowest $h_{9/2}\oplus f_{7/2}$ bands in Fig. 21. The quadrupole deformation β_2 is the value predicted for the lowest $h_{9/2}$ bandhead [35] and corresponds closely to the prolate structures in the even-even neighbors [34]. For the oblate shape ($\gamma=60°$), two simple strongly coupled bands are expected, which clearly disagrees with the experimental pattern of states. For the prolate shape ($\gamma=0°$), a decoupled band pattern results. The best overall agreement is achieved with $\gamma\approx20°$, which provides a good description of the ordering of the energy levels, the splitting between the two lowest bands, and the experimental $B(E2,5/2^-\rightarrow9/2^-)$ rate [1.26(12) e^2 b^2 [30] compared to the PTRM value of 1.22 e^2 b^2].

All states calculated with the PTRM at this deformation and within $\sim$700 keV of the $9/2^-$ bandhead are shown to the left of the dashed line in Fig. 22. The calculated states have been organized into bands of states with roughly similar structure, and the corresponding experimental states are shown in the right panel of that figure. Clearly there is a good general agreement between the data and the calculations. The first calculated states that do not have identified experimental counterparts are the second $7/2^-$ and $3/2^-$ states, which are calculated to lie 412 keV and 504 keV above the $9/2^-$ bandhead, respectively. The calculated and experimental relative γ-ray intensities are compared in Table V, and overall the agreement is quite good. With the excep-

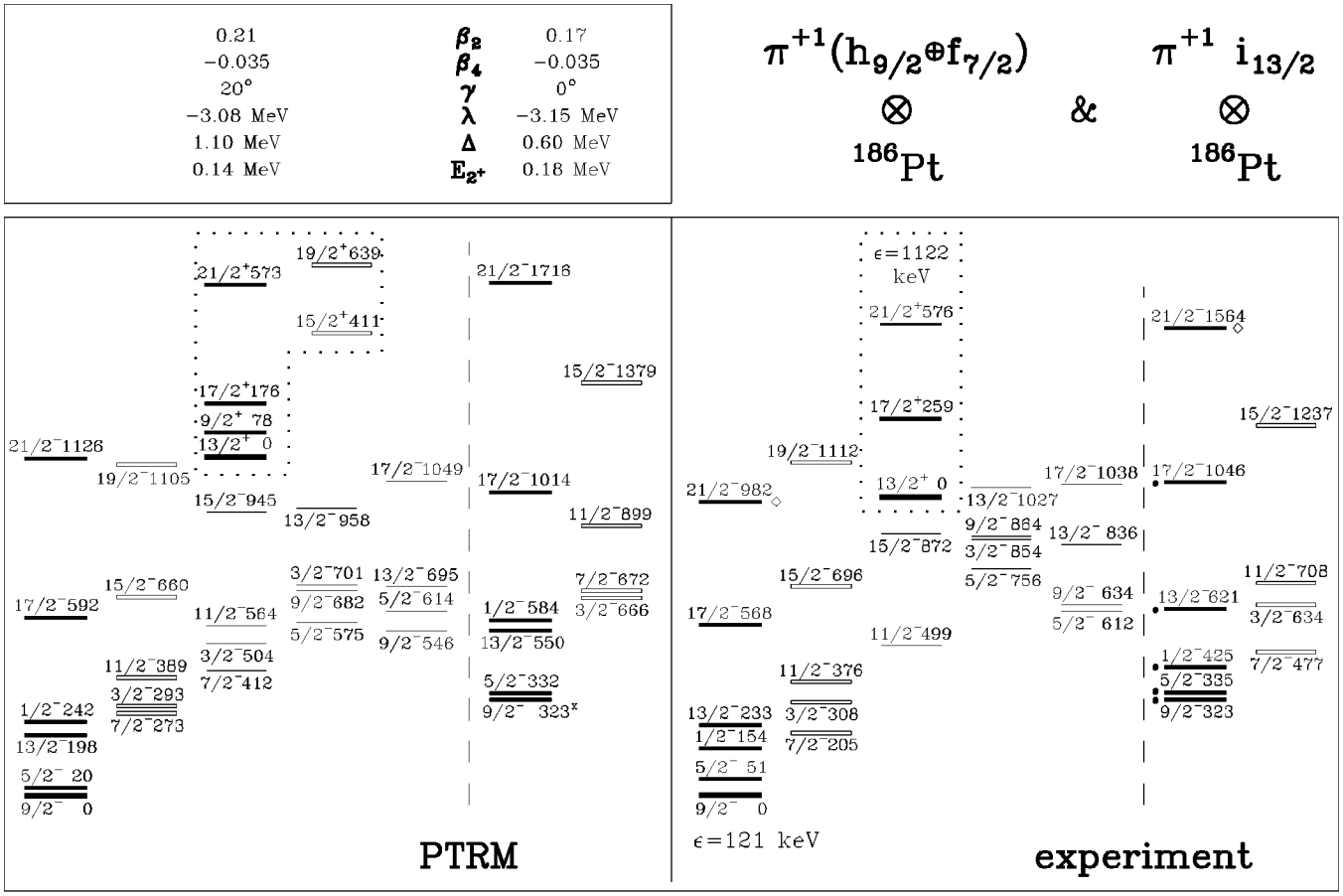

FIG. 22. The negative-parity states $h_{9/2}\oplus f_{7/2}$ and $(h_{9/2}\oplus f_{7/2})'$ (separated by dashed lines), and the $i_{13/2}$ family of positive-parity states (boxed in by the dotted lines) in ^{187}Au. The results of the PTRM calculation are shown on the left and the experimental data on the right. Level energies are given in keV relative to the bandhead energy. The $i_{13/2}$ bandhead is drawn at 1135 keV (PTRM) and 1001 keV (expt.) above the $h_{9/2}\oplus f_{7/2}$ bandhead, but denoted as ''0'' to show that it is another band. The bandhead energy for the calculated intruder band $(h_{9/2}\oplus f_{7/2})'$ is adjusted to be the same as the experimental bandhead energy. Levels with depopulating $E0$ transitions are denoted by a solid circle and those seen in the experimental in-beam data [10,9] by an open diamond. For the definitions of λ, Δ, and E_{2^+} see Fig. 17.

tion of the $3/2_1$ and $13/2_3$ states, the strongest calculated γ-ray transition is also the strongest observed transition in each case. Note also that the second experimental $3/2^-$ state, shown at 854 keV above the $9/2^-$ bandhead in Fig. 22, corresponds to the third calculated $3/2^-$ state, shown at 701 keV. If the second calculated $3/2^-$ state (shown at 504 keV) is instead compared to the observed γ-ray decay pattern of the experimental $3/2^-$ state at 854 keV, the agreement is somewhat worse; in particular, the $3/2^-\rightarrow 5/2_1^-$ transition is calculated to be about 10 times stronger than is observed. Also, the observed decay pattern of the experimental $3/2^-$ state at 634 keV above the $9/2^-$ bandhead (shown to the right of the dashed line in Fig. 22) disagrees considerably from the expected pattern for the second calculated $3/2^-$; this disagreement supports the placement of this $3/2^-$ state in the coexisting $(h_{9/2}\oplus f_{7/2})'$ system described below.

The $i_{13/2}$ band has also been calculated with the same parameters as for the $h_{9/2}\oplus f_{7/2}$ states, and these are shown inside the dotted lines in Fig. 22. The calculated position of the $13/2^+$ bandhead is 1135 keV above the $9/2^-$ bandhead of the $h_{9/2}\oplus f_{7/2}$ states, and this agrees quite well with the experimental position (1001 keV above the $9/2^-$ level). The general pattern of states in the $i_{13/2}$ band is described well by the calculations, and confirms the prolate nature of this band. However, it is difficult to draw more detailed conclusions, e.g., whether an axially symmetric shape with $\gamma=0°$ provides a better description of the $i_{13/2}$ band, based on the present data.

The PTRM calculations provide a good description of the lowest $h_{9/2}\oplus f_{7/2}$ bands, but cannot account for the additional states observed experimentally beginning with the $9/2^-$ level at 323 keV and displayed as the last two bands on the experimental panel in Fig. 22 (to the right of the dashed line). The first important feature of these states, denoted as the $(h_{9/2}\oplus f_{7/2})'$ bands, is that the levels marked with the bullet show $E0$ transitions to the lowest $h_{9/2}\oplus f_{7/2}$ band, while the other states do not. Second, the general pattern of states in the $(h_{9/2}\oplus f_{7/2})'$ bands is remarkably similar to the $h_{9/2}\oplus f_{7/2}$ bands, which implies a prolate or near-prolate $(h_{9/2}\oplus f_{7/2})'$ structure and not the oblate strongly coupled $h_{9/2}$ bands based on the [505]9/2 Nilsson orbital known in the neighboring Tl isotopes [1,36,37], and expected from the axial calculations [35]. An oblate $(h_{9/2}\oplus f_{7/2})'$ band should have a much simpler strong-coupling pattern (see Fig. 21) instead of repeating the decoupled $h_{9/2}\oplus f_{7/2}$ structure seen at low energies. Finally, the moment of inertia is considerably

TABLE V. Calculated and experimental relative γ-ray intensities for the $h_{9/2}\oplus f_{7/2}$ band of ^{187}Au.

Relative I_γ			
Position	E_γ (keV)	PTRM calc.	experiment
$7/2_1^-\rightarrow 9/2_1^-$	205.4	100	100
$7/2_1^-\rightarrow 5/2_1^-$	153.7	29	37.7(45)
$3/2_1^-\rightarrow 5/2_1^-$	256.4	1240	88(13)
$3/2_1^-\rightarrow 1/2_1^-$	153.3	100	100
$3/2_1^-\rightarrow 7/2_1^-$	102.3	32	1.1(6)
$11/2_1^-\rightarrow 9/2_1^-$	376.3	100	100
$11/2_1^-\rightarrow 7/2_1^-$	171.7	1	1.3(37)
$11/2_1^-\rightarrow 13/2_1^-$	142.6	3	5.0(5)
$11/2_2^-\rightarrow 9/2_1^-$	499.4	100	100
$11/2_2^-\rightarrow 7/2_1^-$	294.5	8	3.1(5)
$11/2_2^-\rightarrow 13/2_1^-$	265.9	1	5.6(10)
$11/2_2^-\rightarrow 11/2_1^-$	123	1	
$5/2_2^-\rightarrow 9/2_1^-$	612	3	
$5/2_2^-\rightarrow 5/2_1^-$	561	60	
$5/2_2^-\rightarrow 1/2_1^-$	457.8	100	100
$5/2_2^-\rightarrow 7/2_1^-$	407.8	50	87(20)
$5/2_2^-\rightarrow 3/2_1^-$	304	11	
$9/2_2^-\rightarrow 9/2_1^-$	634.9	59	19(6)
$9/2_2^-\rightarrow 5/2_1^-$	583.4	78	19(6)
$9/2_2^-\rightarrow 7/2_1^-$	429.6	100	100
$9/2_2^-\rightarrow 13/2_1^-$	401	3	
$9/2_2^-\rightarrow 11/2_1^-$	258.7	5	14(5)
$15/2_1^-\rightarrow 13/2_1^-$	462.1	100	100
$15/2_1^-\rightarrow 11/2_1^-$	319.2	27	59.3(35)
$15/2_1^-\rightarrow 11/2_2^-$	196.0	<1	5.5(17)
$15/2_1^-\rightarrow 17/2_1^-$	127.4	1	6.8(17)
$5/2_3^-\rightarrow 9/2_1^-$	756	<1	
$5/2_3^-\rightarrow 5/2_1^-$	705	49	
$5/2_3^-\rightarrow 1/2_1^-$	602	10	
$5/2_3^-\rightarrow 7/2_1^-$	551.8	100	100(43)
$5/2_3^-\rightarrow 3/2_1^-$	449	96	
$5/2_3^-\rightarrow 9/2_2^-$	121	<1	
$3/2_2^-\rightarrow 5/2_1^-$	803.5	1	7.3(15)
$3/2_2^-\rightarrow 1/2_1^-$	700.3	100	100
$3/2_2^-\rightarrow 7/2_1^-$	649	4	
$3/2_2^-\rightarrow 3/2_1^-$	547	15	
$3/2_2^-\rightarrow 5/2_2^-$	243	1	

Relative I_γ			
Position	E_γ (keV)	PTRM calc.	experiment
$13/2_2^-\rightarrow 9/2_1^-$	836.2	54	76.6(54)
$13/2_2^-\rightarrow 13/2_1^-$	602.9	52	50(4)
$13/2_2^-\rightarrow 11/2_1^-$	459.4	100	100
$13/2_2^-\rightarrow 11/2_2^-$	336.7	4	48.9(30)
$13/2_2^-\rightarrow 17/2_1^-$	268	1	
$13/2_2^-\rightarrow 9/2_2^-$	201	2	
$13/2_2^-\rightarrow 15/2_1^-$	140.7	<1	3.2(11)
$9/2_3^-\rightarrow 9/2_1^-$	864.4	21	50(8)
$9/2_3^-\rightarrow 5/2_1^-$	813.3	1	29.2(55)
$9/2_3^-\rightarrow 7/2_1^-$	659.4	100	100
$9/2_3^-\rightarrow 11/2_1^-$	487.7	13	58(11)
$9/2_3^-\rightarrow 11/2_2^-$	365	17	
$15/2_2^-\rightarrow 13/2_1^-$	639.4	100	100
$15/2_2^-\rightarrow 11/2_1^-$	496.5	18	2.3(12)
$15/2_2^-\rightarrow 11/2_2^-$	373.6	71	11(2)
$15/2_2^-\rightarrow 17/2_1^-$	305	1	
$13/2_3^-\rightarrow 9/2_1^-$	1027.3	4	13(4)
$13/2_3^-\rightarrow 13/2_1^-$	795.0	24	34.8(53)
$13/2_3^-\rightarrow 11/2_1^-$	650.9	100	100
$13/2_3^-\rightarrow 11/2_2^-$	527.8	223	97(12)
$13/2_3^-\rightarrow 15/2_1^-$	331.8	10	24(9)
$13/2_3^-\rightarrow 15/2_2^-$	155	8	
$17/2_2^-\rightarrow 13/2_1^-$	805.5	4	94(30)
$17/2_2^-\rightarrow 17/2_1^-$	470.2	100	100
$17/2_2^-\rightarrow 15/2_1^-$	342.8	71	78(20)
$17/2_2^-\rightarrow 13/2_2^-$	202	8	
$19/2_1^-\rightarrow 17/2_1^-$	544.0	100	100
$19/2_1^-\rightarrow 15/2_1^-$	416.9	76	83(22)

smaller for the $(h_{9/2}\oplus f_{7/2})'$ band than for the $h_{9/2}\oplus f_{7/2}$ band. These observations indicate that the excited structure associated with the $9/2^-$ state at 323 keV cannot be explained in terms of the Coriolis mixing of single-particle orbitals at one deformation minimum. In addition, the low energy of this state, 323 keV, cannot be explained in terms of an adiabatic collective excitation (e.g., β or γ vibration) built upon a single shape (in the neighboring even-even Pt isotopes, γ vibrational states appear at $\sim$650 keV).

A separate PTRM calculation performed at a deformation of $\beta_2=0.17$, $\gamma=0°$ is shown to the right of the dashed line in the PTRM panel of Fig. 22. No mixing is included between these different core shapes and the energy splitting between the two sets of states is not calculated but is simply set to 323 keV. The agreement between the calculated and experimental energies of the $(h_{9/2}\oplus f_{7/2})'$ bands is rather good; note, however, that similar results are obtained with a small triaxiality ($\gamma\approx 18°$), and the quadrupole deformation β_2 is not as firmly established as for the lower $h_{9/2}\oplus f_{7/2}$ bands where experimental $E2$ transition rates are available. In any case, the general pattern of states and the smaller moment of inertia clearly establish a prolate or near-prolate $(h_{9/2}\oplus f_{7/2})'$ structure with a smaller deformation than for the lower $h_{9/2}\oplus f_{7/2}$ bands.

Since the PTRM calculations ignore any explicit mixing between the effective cores, it is not possible at present to calculate transitions between the $(h_{9/2}\oplus f_{7/2})'$ and $(h_{9/2}\oplus f_{7/2})$ configurations. However, a qualitative explanation can be offered for the observed pattern of $E0$ transitions between the coexisting states. According to the standard interpretation [38], fast $E0$ transitions (i.e., fast enough to compete favorably with other available decay modes) require a mixing between the underlying coexisting configurations. The effective cores $|A\rangle$ and $|B\rangle$ are linear combinations of the pure configurations $|i\rangle$ and $|g\rangle$, i.e., $|A\rangle=\alpha|g\rangle+\beta|i\rangle$ and $|B\rangle=\alpha|i\rangle-\beta|g\rangle$. The $E0$ transition matrix element between the effective cores is determined by the mixing and the difference in charge radii r_c,

$$\langle B|M(E0)|A\rangle=\alpha\beta[\langle i|(r^2)_c|i\rangle-\langle g|(r^2)_c|g\rangle], \quad (1)$$

assuming that the off-diagonal term $\langle i|(r^2)_c|g\rangle$ vanishes. If an odd particle in a deformed orbital χ_A or χ_B is coupled to these effective cores, then the $E0$ transition is attenuated by the overlap of the single-particle wave functions,

$$\langle\chi_B\otimes B|M(E0)|\chi_A\otimes A\rangle=\langle\chi_B|\chi_A\rangle\langle B|M(E0)|A\rangle. \quad (2)$$

In the PTRM calculations, the odd proton mainly occupies the $h_{9/2}$ orbital in the lowest band of each of the two configurations. Consequently, the overlap of the single-particle wave functions $\langle\chi_B|\chi_A\rangle$ is large, and the core-driven $E0$ transition is not attenuated by the presence of the odd proton. In the first excited band in the $(h_{9/2}\oplus f_{7/2})'$ configuration, the odd proton mainly occupies the $h_{9/2}$ orbital, but the corresponding band in the $(h_{9/2}\oplus f_{7/2})$ configuration has significant $f_{7/2}$ content as well. As a result, there is some mismatch between the single-particle orbitals, and consequently the overlap $\langle\chi_B|\chi_A\rangle$ hinders the $E0$ transitions between these states. This scenario is schematically indicated in Fig. 23.

In the simplest view of particle-core coupling models, it is natural to try to associate the effective core with the physical collective states in the neighboring even-even nuclei, and for these $\pi^{+1}(h_{9/2}\oplus f_{7/2})$ states, the A-1 nucleus ^{186}Pt would be the appropriate reference. Such a simplistic approach neglects changes induced by the presence of the odd particle, e.g., blocking and polarization effects. Shape coexistence is well known in ^{186}Pt, where the ground band is identified as a prolate intruder configuration, and the coexisting normal states are oblate [3,34]. The prolate effective core obtained here for the lower $(h_{9/2}\oplus f_{7/2})$ states in ^{187}Au corresponds well to the ground intruder configuration in ^{186}Pt, but the less-deformed prolate core necessary to describe the $(h_{9/2}\oplus f_{7/2})'$ states clearly does not correspond to the expected coexisting oblate configuration in ^{186}Pt.

The strong similarity between the two effective cores is intriguing; in spite of similar deformations, the intrinsic configurations of the lowest and the excited band structures have to differ structurally. A similar situation is known in the lighter nuclei around ^{176}Pt [39–41], where the experimental data can be interpreted in terms of a low-spin shape coexistence between different shapes associated with $N=5$ proton orbitals intruding from above the $Z=82$ spherical shell closure. The less-deformed structure is calculated [42,43] to involve no $N=5$ ($h_{9/2}$ and $f_{7/2}$) protons and hence is labeled as 5^0. The more deformed structure 5^2, contains a pair of $N=5$ protons coupled to zero angular momentum. The low-spin shape change is strongly favored by the deformed neutron gap at $N=98$. A similar situation can be expected around the deformed neutron gap at $N=108$ [36,37]. The presence of two cores built on the diabatic $|g\rangle=|5^0\rangle$ and $|i\rangle=|5^2\rangle$ configurations offers a plausible explanation to the unusual similarity of the $h_{9/2}\oplus f_{7/2}$ bands in ^{187}Au [17].

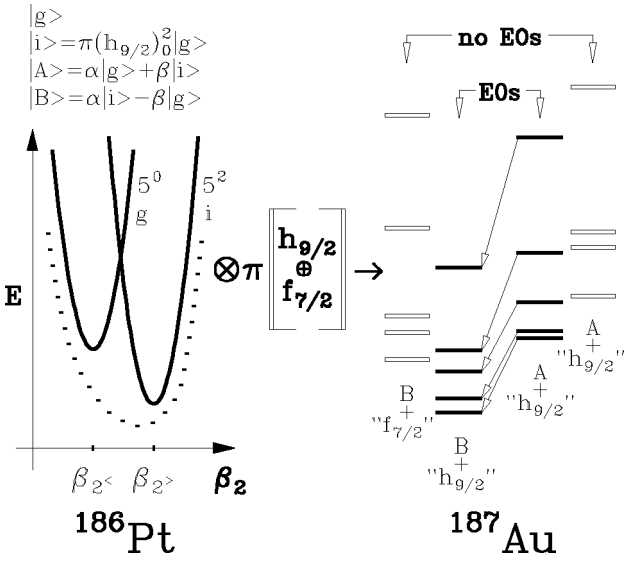

FIG. 23. A schematic illustration of the coupling scheme between the unpaired proton and the effective cores. The underlying core configurations contain 0 (5^0) or 2 (5^2) protons in the $N=5$ intruder orbitals, and the effective cores $|A\ \rangle$ and $|B\ \rangle$ are linear combinations of these. The dotted line indicates the adiabatic potential energy surface constructed from the quasiparticle vacuum state at each deformation, and the solid lines indicate diabatic configurations obtained by removing the interaction between the vacuum and two-quasiparticle states involving $h_{9/2}$ proton configurations.

VI. CONCLUSIONS

By using the experimental instrumentation and techniques developed at UNISOR to search for and quantify electric monopole transitions, it was demonstrated that $E0$ enhancement in transitions between shape coexisting configurations is a common feature and that it can be used as a signature for nuclear shape coexistence. With the connection between $E0$ transitions and nuclear shape coexistence established, a series of experiments on ^{187}Au, by means of β decay of ^{187}Hg^m and ^{187}Hg^g, was initiated. Two things became immediately apparent: first, the spectra were exceedingly complex (more than 500 transitions in ^{187}Au and hundreds of contaminating transitions from other $A=187$ isobars) and, second, the β-decay intensity to the configurations of most interest is small (e.g., $\leqslant$1.6% of the total EC+β^+ feeding from ^{187}Hg^m to the $h'_{11/2}$ band). In order to extract the relevant *physics*, it became obvious that a new level of spectroscopic sensitivity and completeness would be required. Without doubt, this work represents a *benchmark* in that regard and is one of the most complete and detailed spectroscopic analyses of a radioactive decay sequence to date.

Spectroscopic techniques developed by us over the years [32,44] were crucial to accomplish that task.

Nine $E0$ transitions were identified and observed to deexcite both high- and low-spin states that decay to four types of structure identified at low energy in ^{187}Au: positive-parity states based on the mixed $s_{1/2}$, $d_{3/2}$, and $d_{5/2}$ structure (including the ground state) with spins up to $17/2^+$ (at the excitation energy of 1605 keV); positive-parity states based on the $i_{13/2}$ structure with spins up to $17/2^+$ (at the excitation energy of 1381 keV); negative-parity states based on the $9/2^-$ isomeric state ($T_{1/2}$=2.3 s) at 120.5 keV with spins up to $19/2^-$ (at the excitation energy of 1233 keV); and negative-parity states based on the $11/2^-$ isomeric state [$T_{1/2}$=48(2) ns [21]] at 223.9 keV with spins up to $19/2^-$ (at the excitation energy of 1405 keV).

Particle+triaxial rotor model calculations, although restricted to a fixed core shape, nonetheless are useful for characterizing configurations and nuclear shapes. The low-lying positive-parity states are well described in terms of $s_{1/2}$, $d_{3/2}$, and $d_{5/2}$ orbitals coupled to a weakly deformed nearly oblate shape, similar to the heavier odd-mass Au isotopes. Additional positive-parity states are identified and are consistent with a more-deformed prolate core. Similar results are found for the $h_{11/2}$ family of states: the low-lying states are well described with a weakly deformed triaxial shape, and additional states consistent with a prolate core are identified. Coexisting prolate structures are identified in the $h_{9/2} \oplus f_{7/2}$ family of states, and the underlying prolate core configurations are characterized by different occupations of the $N=5$ proton intruder orbitals.

The new, comprehensive, and detailed experimental data presented here for the ^{187}Au nucleus serves as a stimulus for the development of models that explicitly include shape coexistence in the formalism.

ACKNOWLEDGMENTS

We thank the staffs of HHIRF and UNISOR for providing the beam and operation of the isotope separator. We also thank M. O. Kortelahti, H. K. Carter, J. Kormicki, S. Zhu, and C. R. Bingham for their assistance in data acquisition. This work was supported in part by the U.S. DOE Grant and Contract Nos. DE-FG02-96ER40978 (Louisiana State), DE-FG02-96ER40958 (Georgia Tech), DE-FG05-92ER40694 (Tennessee Tech), and DE-AC05-76ORO0033 (UNISOR).

[1] K. Heyde, P. Van Isacker, M. Waroquier, J. L. Wood, and R. A. Meyer, Phys. Rep. **102**, 291 (1983).
[2] J. H. Hamilton, P. G. Hansen, and E. F. Zganjar, Rep. Prog. Phys. **48**, 631 (1985).
[3] J. L. Wood, K. Heyde, W. Nazarewicz, M. Huyse, and P. Van Duppen, Phys. Rep. **215**, 101 (1992).
[4] J. L. Wood, M. O. Kortelahti, E. F. Zganjar, and P. B. Semmes, Nucl. Phys. **A600**, 283 (1996).
[5] C. D. Papanicolopulos, M. A. Grimm, J. L. Wood, E. F. Zganjar, M. O. Kortelahti, J. D. Cole, and H. K. Carter, Z. Phys. A **330**, 371 (1988).
[6] M. O. Kortelahti, E. F. Zganjar, H. K. Carter, C. D. Papanicolopulos, M. A. Grimm, and J. L. Wood, J. Phys. G **14**, 1361 (1988).
[7] A. Korichi, N. Perrin, C. Bourgeois, D. Hojman, D. G. Popescu, H. Sergolle, F. Hannachi, and M. G. Porquet, Z. Phys. A **343**, 15 (1992).
[8] V. P. Janzen *et al.*, Phys. Rev. C **45**, 613 (1992).
[9] J. K. Johansson, D. G. Popescu, D. D. Rajnauth, J. C. Waddington, M. P. Carpenter, L. H. Courtney, V. P. Janzen, A. J. Larabee, Z. M. Liu, and L. L. Riedinger, Phys. Rev. C **40**, 132 (1989).
[10] C. Bourgeois, M. G. Porquet, N. Perrin, H. Sergolle, F. Hannachi, G. Bastin, and F. Beck, Z. Phys. A **333**, 5 (1989).
[11] A. J. Larabee, M. P. Carpenter, L. L. Riedinger, L. H. Courtney, J. C. Waddington, V. P. Janzen, W. Nazarewicz, J.-Y. Zhang, R. Bengtsson, and G. A. Leander, Phys. Lett. **169B**, 21 (1986).
[12] G. Savard *et al.* and the ISOCELE Collaboration, Nucl. Phys. **A512**, 241 (1990).
[13] K. Wallmeroth *et al.*, Phys. Rev. Lett. **58**, 1516 (1987); K. Wallmeroth *et al.*, and the ISOLDE Collaboration, Nucl. Phys. **A493**, 224 (1989).
[14] U. Krönert, St. Becker, G. Bollen, M. Gerber, Th. Hildebrath, H.-J. Kluge, G. Passler, and the ISOLDE Collaboration Z. Phys. A **331**, 521 (1988).
[15] B. Hinfurtner, E. Hagn, E. Zech, R. Eder, the NICOLE Collaboration, and the ISOLDE Collaboration, Phys. Rev. Lett. **67**, 812 (1991).
[16] G. Passler, J. Rikovska, E. Arnold, H. J. Kluge, L. Monz, R. Neugart, H. Ravn, K. Wendt, and the ISOLDE Collaboration, Nucl. Phys. **A580**, 173 (1994).
[17] D. Rupnik, E. F. Zganjar, J. L. Wood, P. B. Semmes, and W. Nazarewicz, Phys. Rev. C **51**, R2867 (1995).
[18] C. Bourgeois, P. Kilcher, J. Letessier, V. Berg, M. G. Desthulliers, and the ISOCELE Collaboration, Nucl. Phys. **A295**, 424 (1978); C. Bourgeois, P. Kilcher, and A. Wojtasiewicz, Orsay Report No. IPNO-DRE-83-33.
[19] M. A. Grimm, Ph.D. thesis, Georgia Tech, 1978.
[20] R. A. Braga, B. E. Gnade, R. W. Fink, and H. K. Carter, Nucl. Phys. **A410**, 441 (1983).
[21] V. Berg, Z. Hu, J. Oms, C. Ekström, and the ISOCELE Collaboration, Nucl. Phys. **A410**, 445 (1983).
[22] V. Berg, J. Oms, K. Fransson, Z. Hu, and the ISOCELE Collaboration, Nucl. Phys. **A453**, 93 (1986).
[23] M. A. Deleplanque, C. Gerschel, M. Ishihara, N. Perrin, V. Berg, C. Bourgeois, M. G. Desthuilliers, J. P. Husson, P. Kilcher, and J. Letessier, J. Phys. (Paris) **36**, L-205 (1975).
[24] C. Ekström, L. Robertsson, S. Ingelman, G. Wannberg, I. Ragnarsson, and the ISOLDE Collaboration, Nucl. Phys. **A348**, 25 (1980).
[25] D. Rupnik, Ph.D. thesis, Louisiana State University, 1994.
[26] J. L. Wood and E. F. Zganjar (unpublished).
[27] E. H. Spejewski, R. L. Mlekodaj, and H. K. Carter, Nucl. Instrum. Methods Phys. Res. **186**, 71 (1981).
[28] R. L. Mlekodaj, E. F. Zganjar, and J. D. Cole, Nucl. Instrum.

Methods Phys. Res. **186**, 239 (1981).
[29] ''HHIRF Computer Handbook,'' Oak Ridge National Laboratory Report, 1987.
[30] R. B. Firestone, Nucl. Data Sheets **62**, 159 (1991).
[31] F. Rösel, H. M. Fries, K. Alder, and H. C. Pauli, At. Data Nucl. Data Tables **21**, 89 (1978).
[32] E. F. Zganjar, J. D. Cole, J. L. Wood, and M. A. Grimm, in ''Proceedings of the 4th International Conference on Nuclei Far From Stability,'' Helsingør, Denmark, edited by P. G. Hansen and O. B. Nielsen, CERN Report 81-09, p. 630; and E. F. Zganjar, M. O. Kortelahti, J. L. Wood, and C. D. Papanicolopulos, in *Nuclei Far From Stability: Fifth International Conference*, edited by I. S. Towner, AIP Conf. Proc. No. **164** (AIP, New York, 1988), p. 313.
[33] S. E. Larsson, G. A. Leander, and I. Ragnarsson, Nucl. Phys. **A307**, 189 (1978).
[34] R. Bengtsson, T. Bengtsson, J. Dudek, G. Leander, W. Nazarewicz, and Jing-ye Zhang, Phys. Lett. **183B**, 1 (1987).
[35] W. Nazarewicz, M. A. Riley, and J. D. Garrett, Nucl. Phys. **A512**, 61 (1990).
[36] W. Reviol *et al.*, Phys. Rev. C **49**, R587 (1994).
[37] G. J. Lane *et al.*, Phys. Lett. B **324**, 14 (1994); G. J. Lane, G. D. Dracoulis, and A. P. Byrne, P. M. Walker, A. M. Baxter, J. A. Sheikh, and W. Nazarewicz, Nucl. Phys. **A586**, 316 (1995).
[38] K. Heyde and R. A. Meyer, Phys. Rev. C **37**, 2170 (1988).
[39] G. D. Dracoulis, A. E. Stuchbery, A. P. Byrne, A. R. Poletti, S. J. Polleti, J. Gerl, and R. A. Bark, J. Phys. G **12**, L97 (1986).
[40] R. Bengtsson, J.-y. Zhang, J. H. Hamilton, and L. K. Peker, J. Phys. G **12**, L223 (1986).
[41] J. Gascon *et al.*, Nucl. Phys. **A470**, 230 (1987).
[42] R. Bengtsson, Nucl. Phys. **A520**, 201c (1990).
[43] B. Cederwall *et al.*, Z. Phys. A **337**, 283 (1990).
[44] E. F. Zganjar, J. L. Wood, and J. Schwarzenberg, in *Proceedings of a Symposium on Exotic Nuclear Spectroscopy*, Miami Beach, Florida, 1989, edited by W. C. McHarris (Plenum Press, New York, 1990), p. 39.